

AC-Yield

An investigation into cooling of modules in floating PV systems and light penetration in land-based solar parks.

Final Report





Authors: Maarten Dörenkämper, Minne de Jong, Simona Villa, Bas van Aken, Oguzhan Apaydin, Willem Biesheuvel

Date: June 2022

This project was co-funded by TKI-Energie from the Topconsortia voor Kennis en Innovatie (TKI's) of the Dutch Ministry of Economic Affairs and Climate.



Summary

In recent years the number of large-scale solar parks strongly increased. This not only increases the solar energy produced, but also the impact on the landscape, ecology and biodiversity. TNO has developed a yield model for solar energy installations, BIGEYE, which simulates light falling on the PV modules for different system designs, which in term is used to simulate the energy produced. This model is adapted to simulate the light falling under the modules, which is a key ingredient to sustain soil quality, ecology and biodiversity. Although this is a powerful tool, the model had not been validated.

In this project, Groenleven and TNO worked together to extend, improve, validate and calibrate the model. For this purpose TNO measured the light falling under PV modules in a commercial solar park of Groenleven. Groenleven facilitated the measurement. These measurements were used to calibrate and validate the simulation software. Investigations show that a number of phenomena are important to include in the light penetration simulations that were not included before. We have shown that specular reflections from surrounding modules and diffuse rear side reflections play an important role. Furthermore we experimented with a variable albedo on the ground. This is a useful addition for currently ongoing and future projects that involve nature inclusive solar parks and agrivoltaic solar farms. With this tool we can quantitively show the effects of design choices for both energy output and under-module soil irradiation. We have shown that both the energy yield calculations and the ground irradiance simulations show the best performance for the semi-transparent bifacial module. This means that for a given minimum irradiance or minimum kWh per unit area demand, with a bifacial module you can achieve the soil quality with a higher coverage of solar panels. Alternatively, you can achieve the energy performance demand with fewer modules per area due to the bifacial gain and have a higher soil irradiance.

A second goal of the project was to quantify the so-called cooling effect of floating PV systems. Previous studies have shown that PV modules are cooler when they are deployed above water, but accurate modelling was not yet available. A new thermal module for the existing model was developed that not only takes into account irradiance and ambient temperature, but also water temperature. This model was calibrated and validated using data that we collected at a commercial floating solar of Groenleven near Oosterwolde, which includes a reference system on land for direct comparison of the PV module temperatures. We found that the influence of ambient temperature and water temperature are strongly intercorrelated and therefore adding water temperature to the model does not increase the accuracy. We did not find significant edge effects, such that the modules near the edges of the system were cooler than the modules near the centre of the system. We did find that cooling due to wind is slightly higher for floating systems, which results in an annual simulated yield increase of 0.8%.

TNO has incorporated the new acquired knowledge into the BIGEYE model. With the newly acquired properties of the model, new types of projects can be initiated in the PV sector, i.e. projects that include soil irradiation simulations or floating PV systems.



Table of Contents

Sı	ummary	<i>/</i>		2
1	Intro	oduct	tion	5
	1.1	Goa	l of the project	5
2	Mea	sure	ment setups	7
	2.1	Floa	ting PV park Weperpolder	7
	2.1.	1	Weather parameters	8
	2.1.	2	Irradiation	8
	2.1.	3	Module temperatures	9
	2.1.	4	Water temperatures	9
	2.1.	5	Under-module air temperatures	9
	2.2	Land	d based park Houtwal	9
	2.2.	1	Light penetration measurements	10
	2.2.	2	Rear side irradiation measurements	10
3	The	rmal	modelling for floating PV	11
	3.1	Mea	surements Weperpolder	11
	3.1.	1	Setup Weperpolder data availability	11
	3.1.	2	Module temperatures	11
	3.2	Yield	d model adapted for FPV module temperatures	20
	3.2.	1	Model build-up	21
	3.2.	2	Model validation	22
	3.2.	3	Modelling results	26
4	Irra	dianc	e modelling	30
	4.1	Intro	oduction	30
	4.2	Арр	roach	30
	4.3	Mod	del validation	31
	4.3.	1	Albedo variation	31
	4.3.	2	Back sheet reflection	34
	4.3.	3	Contribution of reflections on sensors	35
	4.3.	4	Specular reflection	36
	4.3.	5	Table (simulation) size	36
	4.3.	6	Gap between modules	38
	4.3.	7	Sources of rear and ground irradiance	39
	4.4	Con	clusions	40
5	Busi	ness	modelling	41



	5.1 Land	d based solar	41
	5.1.1	Assumptions	41
	5.1.2	Results	41
	5.2 Floa	ting solar	42
		Assumptions	
		Results	
6		A – Availability all individual sensors Weperpolder	



1 Introduction

In the past years the number of large-scale solar parks strongly increased. The effect is clearly seen in our living area and as a result the opposition to these parks is growing. Not only the visual appearance is often mentioned in the debate, but the effect on the biodiversity is becoming an important topic in the discussion as well. This holds both for parks on land as well as on water. However, there is not much known on the effect of solar parks on biodiversity. The discussion so far is mainly based on feelings and perception and not on scientific based evidence. To be able to make predictions of plant growth and biodiversity under solar modules, a better understanding of light distribution below the solar modules in a solar park is needed. The rationale here is that we should avoid spots under the solar modules that receive no or very little light. As very little is known on this topic, proper modelling is needed. TNO has developed a modelling approach for under-module light penetration, and incorporated into the BIGEYE simulation toolset. Up till now, these simulations were not validated. In the AC-Yield project, we performed measurements on light reaching the soil beneath the solar tables, to validate the model. Furthermore, we improve the model using the validation analysis. In this way we can find out which effects need to be included in the model to reach an acceptable accuracy, balanced against model building and computational efforts.

For land based parks, we use the same BIGEYE modelling approach to model the additional yield of using bifacial solar modules. To validate these simulations, we performed measurements on light reaching the rear side of the modules. Again, in this way we can find out which effects need to be included in the model to reach an acceptable accuracy, balanced against model building and computational efforts.

PV modules deployed above water are believed to be cooler than the same module in land-based parks, leading to a higher energy output. A number of investigations have been performed on this so-called cooling effects, but these were all focused on pilot sized systems. To better understand the economic consequences of the cooling effect, it is crucial to understand cooling in commercial size floating PV systems, including temperature distribution, the influence of wind and of water temperature. For this purpose we develop a model to simulate the PV temperature of floating PV systems. In turn we calibrate and validate the model with data gathered at a commercial sized floating PV park.

1.1 Goal of the project

In this project the BIGEYE annual yield model as developed by TNO¹ for predicting the energy yield of solar parks is used for a first step to estimate the effect on biodiversity. By adapting the model, the ground irradiance can be modelled, giving insight in the amount of sunlight that reaches the ground between and under the panels. This irradiance was measured in the project to validate the model. The results can be used to estimate the irradiance at the water level in floating parks as well.

M. Klenk, H. Nussbaumer, T. Baumann, 35th EU PVSEC 2018, Brussels, Belgium, 24-28 September 2018

¹ G.J.M. Janssen, A.R. Burgers, A. Binani, A.J. Carr, B.B. Van Aken, I.G. Romijn



The goal of the project is the development of a validated model to predict energy penetration and backside irradiation of PV modules in a land-based solar park. In the model, several light scattering effects, reflection, absorption and transparency will be included and evaluated.

A second goal is to build a validated model that describes the cooling effect of PV modules deployed on water.

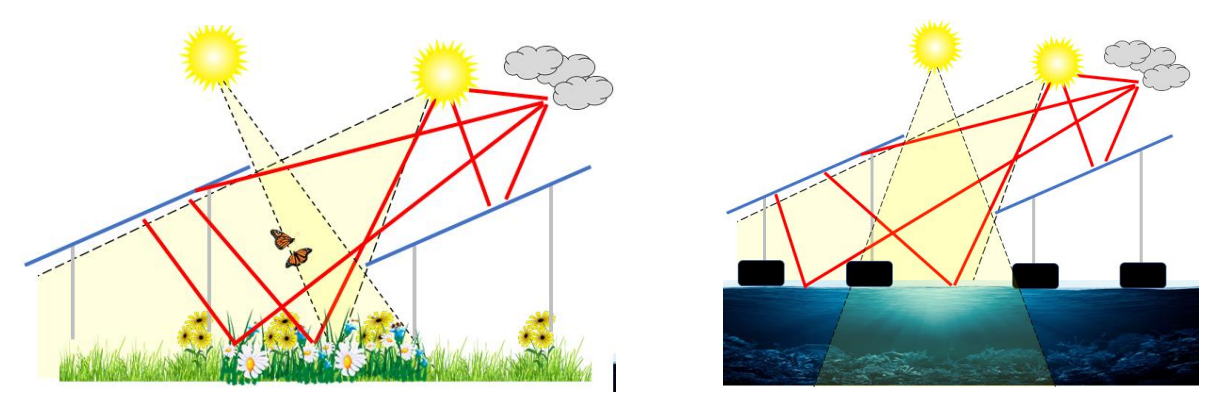


Figure 1: Left PV on land, right PV on water. Red lines indicate the different sun beams that contribute to electricity generation and ground irradiance. These contributions are measured and modelled in this project.

This combined with the surface irradiance calculations under and between the solar panels as developed in the IMBYP project will result in a validated and solid model that can contribute to:

- Improve the bankability of PV on land and water
- Optimize solar park settings for esthetics and biodiversity and determine the effect of those on the energy yield
- A better understanding of the cooling effect of floating PV systems for large scale systems, and the additional energy output due to the cooling of the modules



2 Measurement setups

Two measurement setups were designed, purchased and built up in two locations. A measurement setup that focusses on module temperatures was built at the floating PV park at Weperpolder. A measurement setup focused on light penetration and backside illumination was built at the Houtwal land-based park. Both parks are situated near the village of Oosterwolde and are governed by GroenLeven.

Both measurement setups primarily make use of wireless data acquisition. A central receiver is placed in a strategic position. The different sensors are wired to data acquisition boxes that communicate wirelessly with the central receiver. In this way, no wires are running over the systems. Especially in the floating system this is a large advantage. When all sensors would be wired to a central location, a large number of wires would be going over the system, resulting in high costs for the system, lower accuracies, large build-up effort and potential unsafe situations.



Figure 2: Location of both solar parks near Oosterwolde

2.1 Floating PV park Weperpolder

The floating solar park at the Weperpolder is the first system built by Groenleven and consists of one unit of their modular floating PV park system. The total park has a rated power of 2.1 MWp. Modules are oriented east and west at an angle of 12°. On shore, close to the park, a smaller reference system was built, using the same system, orientation and tilt. This smaller system serves a reference to the on-water measurements. The park is built on a sand extraction lake. The figure below shows a part of the park and its surroundings.



Figure 3: The Weperpolder floating PV park

The measurement setup consists of several components, measuring weather parameters, irradiation in different orientations, module temperatures, water temperatures and under-module temperatures. Figure 4 gives an overview of the different sensors and measurement equipment placed on the system and the reference system. All data is either wired or wirelessly collected in a central measurement cabinet. This cabinet communicates with our central data server. Data is locally stored and uploaded to our central server every 24 hours.

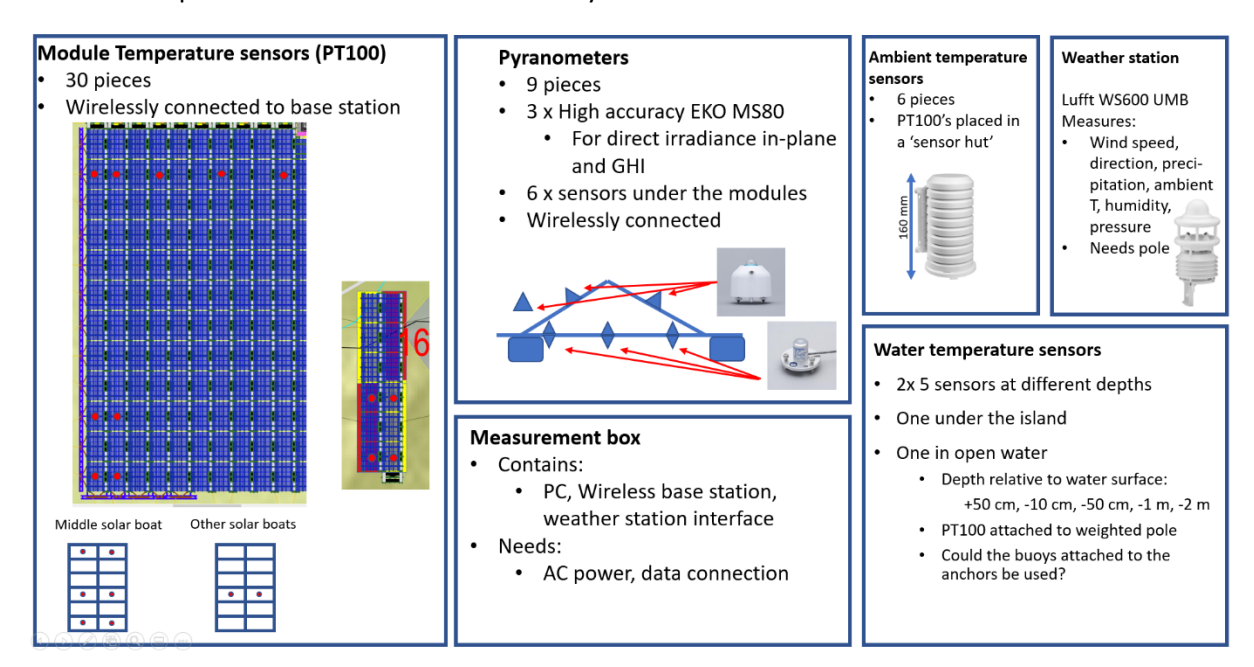


Figure 4: An overview of the different sensors and measurement equipment placed on the floating PV system and the reference system

2.1.1 Weather parameters

For measuring weather parameters we deployed a Lufft WS600 UMB weather sensor, measuring wind speed and direction, ambient temperature, precipitation, relative humidity and air pressure. It is directly connected to our central measurements box and stores measurements on a 1-minute interval.

2.1.2 Irradiation

Several irradiation sensors were placed to measure the incoming sunlight in different planes. Three EKO MS-80 units were placed to measure Global Horizontal Irradiance (GHI) and in-plane irradiation



in the plane of the modules in high accuracy. These sensors are placed near the centre of the system. Six EKO ML-1 silicon sensors were placed under the modules in one of the 'boats', to measure light penetration under the modules. All sensors wirelessly communicate with the central receiver. Datapoints are stored with 2-minute intervals.

2.1.3 Module temperatures

Under 30 modules surface temperature sensors were placed. We used 3-terminal PT100 sensors. Sensors were placed on four 'boats' in the southwest corner of the island, and in an inward going series near the middle of the island. On the reference modules on land, sensors were placed in the orientation as the southwest corner. The sensors communicate wirelessly with the central receiver. Datapoints are stored with 2-minute intervals.

Figure 4 gives the position of the different sensors.

2.1.4 Water temperatures

Knowing the water temperature is crucial to understand the cooling effect of water on the PV modules. Therefore we monitor the water temperature. For ecological reasons it is interesting to monitor the water temperature at different depths. Therefore water temperature sensors (3-terminal PT100s) were placed at 20, 50, 100 and 200 centimeter depths, in two locations. One measurement set was placed in the centre of the system and one was placed just outside the edge of the system.

2.1.5 Under-module air temperatures

In six strategic positions, temperature sensors were placed in sensor huts to measure the air temperature under the PV modules, using 3-terminal PT100s. Two under-module air temperature sensors were placed under the reference modules.

2.2 Land based park Houtwal

The land-based solar park 'Houtwal' is situated just outside Oosterwolde in the Friesland province. It has an installed power of 50 MW. The modules are oriented southeast and placed on tables in the 3-portrait orientation.



Figure 5: A view on a part of the Houtwal land-based solar park

To investigate the light penetration under the modules and the rear side irradiation of the modules, light sensors were placed near the ground facing up, and near the rear of the modules facing down. The sensors communicate wirelessly with a central cabinet, which in turn communicates with our



central data server. Data is stored in 2-minute intervals, stored locally and uploaded every 24 hours to the central server.

2.2.1 Light penetration measurements

To measure the light penetration under the modules, a row consisting of ten EKO ML-01 irradiance sensors, facing up horizontally, was placed under the modules. The first and last sensor were placed so that they are situated half a meter putside the solar tables on both sides. The other sensors are evenly distributed in between. Figure 6 shows the sensors as installed in the solar park.



Figure 6: Light penetration sensors placed at the Houtwal land-based solar park.

2.2.2 Rear side irradiation measurements

A set of 10 EKO ML-01 irradiance were placed under the modules, evenly distributed over the rear face of the modules. The orientation is in-plane with the modules. Figure 7 shows the sensors as installed in the solar park.



Figure 7: Rear side irradiation sensors at the Houtwal land-based solar park.



3 Thermal modelling for floating PV

3.1 Measurements Weperpolder

3.1.1 Setup Weperpolder data availability

Measurements of the so called "remote-sensors" in the Weperpolder started at the 20th of October in 2020. The Weather station was put into operation a few months later on the first of April 2021. In Figure 8 one can find a bar chart, which illustrates the availability of the two data-loggers ("Weatherstation" and "remote-sensors"). It can be seen that, besides the non-simultaneous start-up, gaps in the data are present. The first data-gap in the summer of 2021 was caused due to non-availability of the grid due to maintenance work of the local grid operator, which meant there was no power on site. The second data-gap occurred in November 2021 and was caused by tripped circuit breakers. Furthermore, occasionally the wireless communication between the central data-logger and some of the individual sensor failed. This caused that during the project the data-transfer of some individual sensors was lost. In Appendix A one can find a chart showing the availability of each individual sensor during the project. As a consequence data of some sensors could not be used at all due to the strong difference in data-set time compared to the well-functioning sensors. This will be discussed in the different sub-sections of this chapter.

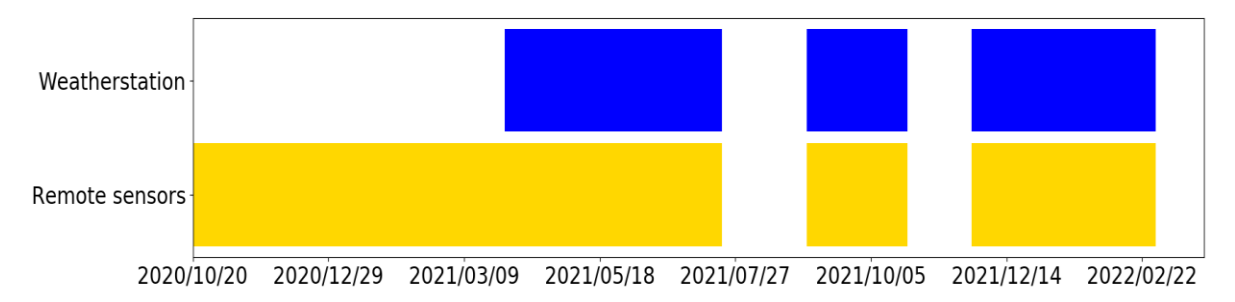


Figure 8: Availability of the two data-loggers over time.

3.1.2 Module temperatures

3.1.2.1 Temperature gradient FPV system

To investigate the temperature gradient over the FPV system, the module temperature of multiple panels over a central West-East axis have been recorded, as described in Section 2.1.3. As the measurements of the module temperature of some panels failed throughout the duration of the project, two different time periods have been identified as most interesting to investigate. The first time period starts at the 1st of April 2021 and ends the 20th of July 2021. During this period the temperatures of most different panels over the central west-east axis could be studied. The position of the different panels can be found in Figure 9. The investigated panels are: 6,12,16,20 (East orientation) and 13,15,17 (West orientation). The second investigated period also start at the first of April and ends almost one year later on the first of March 2022. During this period the temperature of the same panels, except for panels 6 and 17, has been investigated.

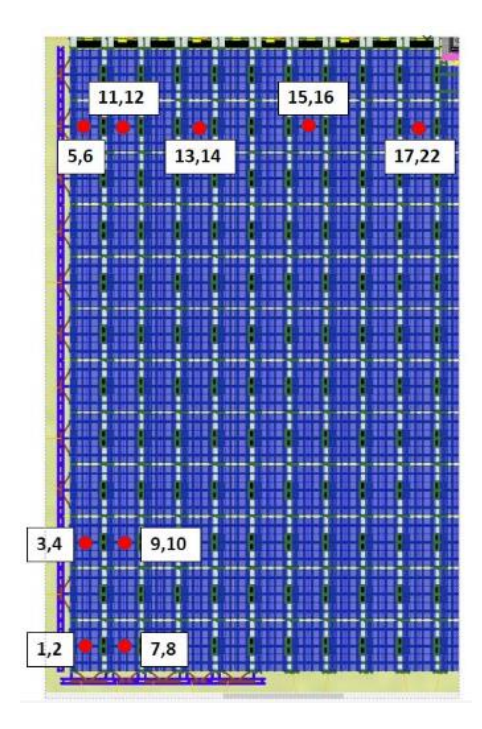


Figure 9: Location of the different investigated PV panels on the Floating PV system. Panels with an even number are orientated towards the East, panels with an odd number are orientated towards the west.

A straightforward method to compare measured temperatures of the panels with each other is to calculate the so-called Irradiance-Weighted Average Temperature (IWAT):

$$T_{IWAT} = \frac{\sum (G_{POA} \cdot T_{mod})}{\sum G_{POA}}$$

where G_{POA} is the plain-of-array irradiance in W/m² and T_{mod} is the measured module temperature in °C. As this average temperature is weighted with irradiance, datapoints with high irradiance have a larger impact compared to datapoints with low irradiance. The performance of the PV panels is roughly linear with irradiance, which make this IWAT method very suitable to give a first insight into the thermal behavior of the FPV system. In Table 1 one can find the calculated IWAT temperature.

Table 1: Irradiance weighted average temperatures on selected panels from west towards east for two different time-periods

Dataset time	Wind	Panel	Orientation	IWAT [°C]
	direction			
2021/04/01 - 2021/07/20	All	6	East	29.0
2021/04/01 - 2021/07/20	All	12	East	28.9
2021/04/01 - 2021/07/20	All	16	East	29.0
2021/04/01 - 2021/07/20	All	20	East	30.2
2021/04/01 - 2021/07/20	All	13	West	29.8
2021/04/01 - 2021/07/20	All	15	West	29.7
2021/04/01 - 2021/07/20	All	17	West	27.0
2021/04/01 - 2022/03/01	All	12	East	26.1
2021/04/01 - 2022/03/01	All	16	East	26.2
2021/04/01 - 2022/03/01	All	20	East	27.2
2021/04/01 - 2022/03/01	All	13	West	27.0
2021/04/01 – 2022/03/01	All	15	West	26.9



Panels with the lower numbers are located more towards the edge of the system, the higher numbers are more situated in the middle of the FPV system. As can be seen in the table above, the differences in IWAT temperature of the different panels are small. Therefore no clear trend can be distinguished.

To investigate to what extend the wind direction has an influence on the gradient of the panel temperature over the FPV system, the datasets are filtered on wind direction. In Figure 10 below one can find the wind-rose diagrams of the two different dataset periods. It can be seen that in the first dataset period the wind direction to a large extend was North-East. In the second dataset period the wind direction is predominantly West. Also the strongest winds are coming from the west.

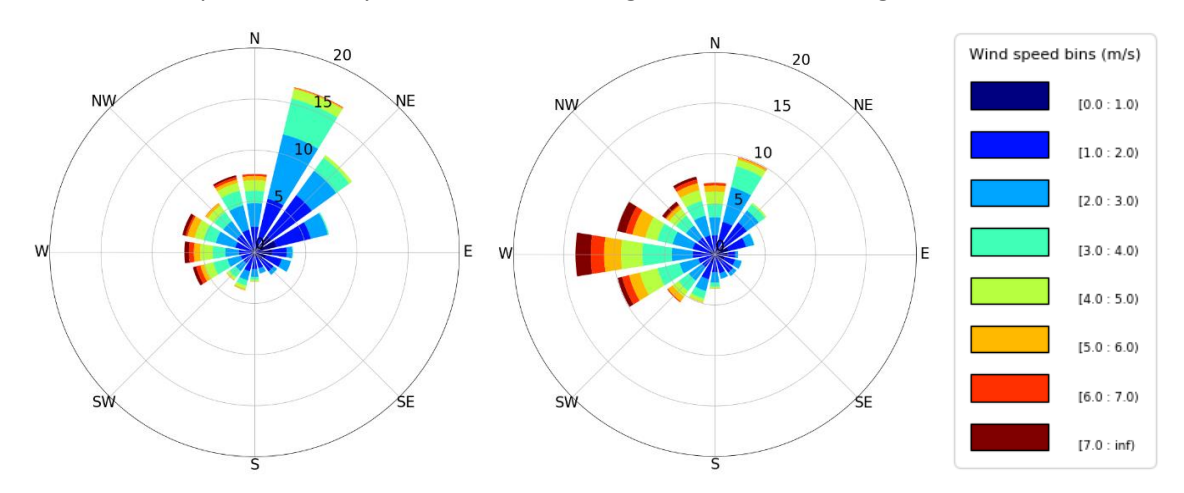


Figure 10: Wind rose diagram over the dataset period 2021/04/01 - 2021/07/20 (left) and the dataset period 2021/04/01 - 2022/03/01 (right).

In the table below the IWAT temperatures can be found, when only data with the wind direction between 225° and 315° (Wind direction: West) has been taken into consideration. Again, the difference in temperature are small. A very small trend can be observed on the panels with an east orientation, where the panels installed more towards the western edge of the system have a slightly lower IWAT. For the panels with a west orientation this is also the case during the second dataset period, but surprisingly not during the first dataset period. The differences in IWAT temperatures are very small. This suggests that the temperature gradient of this large scale FPV system does not play a major role in the electrical performance of the system.

Table 2: Irradiance weighted average temperatures on selected panels from west towards east for two different timeperiods filtered on wind direction

Dataset time	Wind direction	Panel	Orientation	IWAT [°C]
2021/04/01 – 2021/07/20	West	6	East	28.4
2021/04/01 - 2021/07/20	West	12	East	28.5
2021/04/01 - 2021/07/20	West	16	East	29.1
2021/04/01 - 2021/07/20	West	20	East	29.6
2021/04/01 - 2021/07/20	West	13	West	28.4
2021/04/01 - 2021/07/20	West	15	West	27.9
2021/04/01 - 2021/07/20	West	17	West	27.3
2021/04/01 - 2022/03/01	West	12	East	24.3
2021/04/01 - 2022/03/01	West	16	East	24.6
2021/04/01 - 2022/03/01	West	20	East	25.0
2021/04/01 - 2022/03/01	West	13	West	24.2
2021/04/01 - 2022/03/01	West	15	West	26.8



Another way to express the different temperature behavior between the floating structures and the reference system is to calculate the heat loss coefficient, generally referred to as the U-value. The higher the U-value, the easier it is for the module to dissipate its thermal energy. The U-value is calculated using:

$$U = \frac{\alpha \cdot G_{POA} \cdot (1 - \eta)}{T_{mod} - T_{amb}}$$

where U is the heat loss coefficient in W/m²K, α is the fraction of the solar spectrum absorbed, G_{POA} is the in-plane irradiance in W/m² and η is the power conversion efficiency of the module. This total U-value can be split into two parts, a constant part and a wind-dependent part, see

$$U = U_C + \nu \cdot U_{\nu}$$

where U is the total heat loss coefficient in W/m²K, U_c is the independent heat loss coefficient, v is the wind speed in m/s and U_v is the wind-dependent heat loss coefficient in W/m²K/m/s

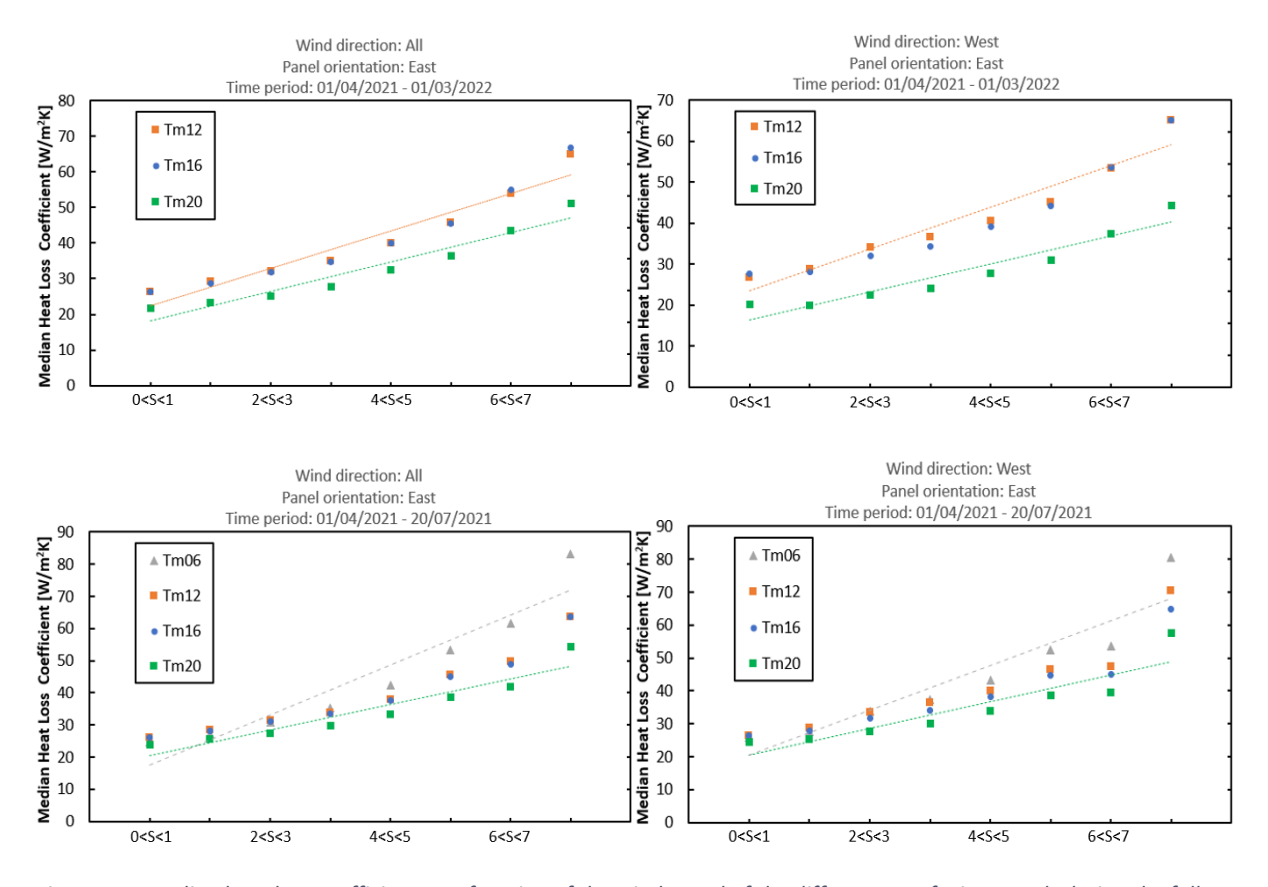


Figure 11: Median heat loss coefficient as a function of the wind speed of the different east facing panels during the full measurement campaign (top row) and between 1/04/2021 until 20/07-2021 (bottom row). All wind directions have been taken into account in the left column, and only the west wind-direction in the column on the right-side.



Table 3: Median total heat loss coefficients U_c and the wind-dependent heat loss coefficients U_c and the wind-dependent heat loss coefficient U_v of the different east facing panels

Dataset time	Wind direction	Panel	U-value [W/m²K]	Uc-value [W/m²K]	Uv-value [W/m²K/m/s]	R ²
2021/04/01 - 2021/07/20	All	Tm06	30.9	14.5	7.5	0.92
2021/04/01 - 2021/07/20	All	Tm12	31.3	21.2	4.5	0.96
2021/04/01 – 2021/07/20	All	Tm16	31.3	21.9	4.1	0.97
2021/04/01 – 2021/07/20	All	Tm20	28.0	20.1	3.5	0.96
2021/04/01 - 2021/07/20	West	Tm06	36.4	19.9	5.7	0.94
2021/04/01 - 2021/07/20	West	Tm12	35.8	22.3	4.5	0.91
2021/04/01 - 2021/07/20	West	Tm16	33.9	21.7	4.1	0.88
2021/04/01 - 2021/07/20	West	Tm20	30.2	19.8	3.6	0.84
2021/04/01 - 2022/03/01	All	Tm12	32.1	17.2	5.3	0.93
2021/04/01 - 2022/03/01	All	Tm16	32.0	16.4	5.5	0.92
2021/04/01 - 2022/03/01	All	Tm20	28.8	15.9	4.6	0.94
2021/04/01 - 2022/03/01	West	Tm12	35.8	18.3	5.1	0.93
2021/04/01 - 2022/03/01	West	Tm16	34.3	17.4	5.1	0.91
2021/04/01 - 2022/03/01	West	Tm20	31.0	16.7	4.4	0.91

Figure 11 depicts the median heat loss coefficients of the different east facing panels as a function of the wind speeds, separated by dataset and wind direction. The different types of heat loss coefficients (total heat loss coefficient U_c independent heat loss coefficient U_c and the wind dependent heat loss coefficient U_c belonging to these plots can be found in Table 3. In general it can be stated that there is a small trend, where the panels towards the western edge of the system show a higher heat loss coefficient. When only times are taken into account, when the wind-direction was west, this gradient effect is slightly larger. Two mechanisms can contribute to this. The wind speed on the edge of the system is somewhat higher compared to the local wind speed in the center of the FPV system. A second possible explanation is that the surrounding panels influence each other. Differences however are small. No significant difference in electrical performance can be expected based on these values.



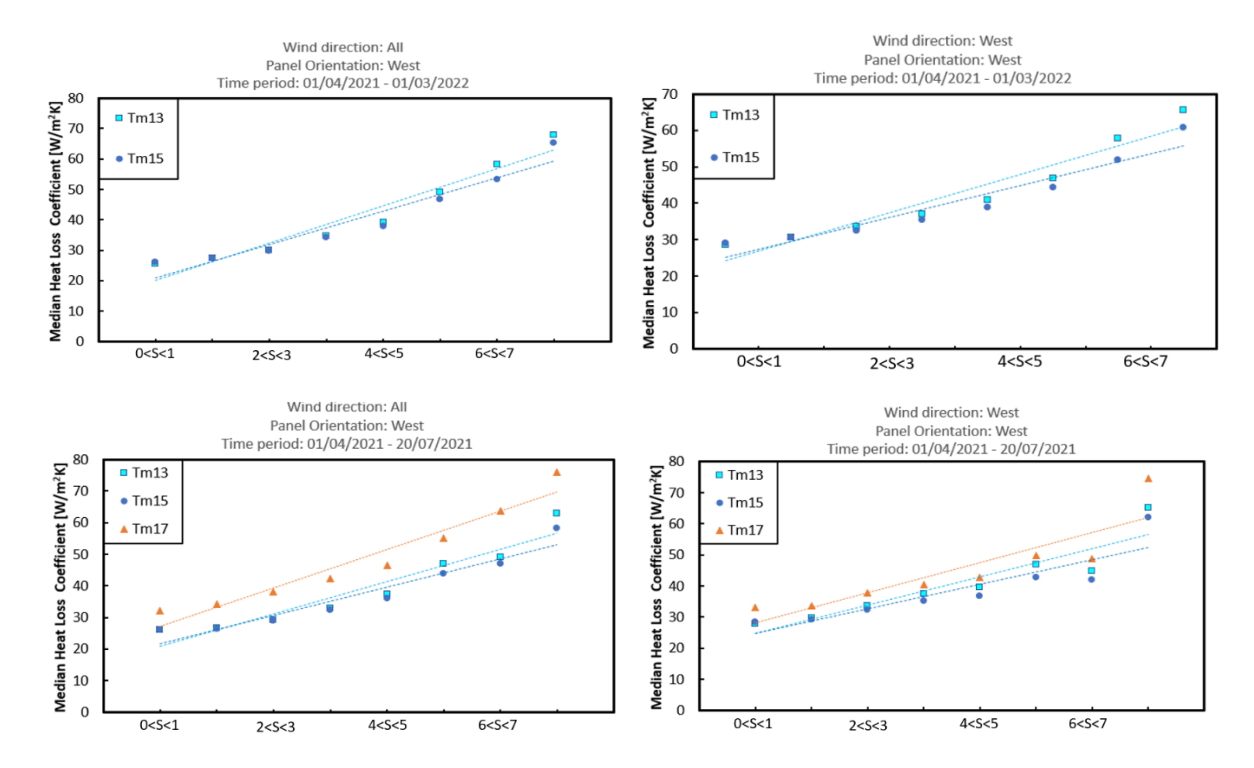


Figure 12: Median heat loss coefficient as a function of the wind speed of the different west facing panels during the full measurement campaign (top row) and between 1/04/2021 until 20/07-2021 (bottom row). All wind directions have been taken into account in the left column, and only the west wind-direction in the column on the right-side.

Table 4: Median total heat loss coefficients U_c and the wind-dependent heat loss coefficients U_c and the wind-dependent heat loss coefficient U_v of the different west facing panels

Dataset time	Wind direction	Panel	U-value [W/m²K]	Uc-value [W/m²K]	Uv-value [W/m²K/m/s]	R ²
2021/04/01 - 2021/07/20	All	Tm13	29.8	18.5	5.1	0.92
2021/04/01 - 2021/07/20	All	Tm15	29.4	19.5	4.5	0.92
2021/04/01 - 2021/07/20	All	Tm17	38.1	24.2	6.1	0.93
2021/04/01 - 2021/07/20	West	Tm13	36.8	22.6	4.5	0.85
2021/04/01 - 2021/07/20	West	Tm15	35.0	22.8	4.0	0.80
2021/04/01 - 2021/07/20	West	Tm17	40.3	25.8	4.8	0.77
2021/04/01 - 2022/03/01	All	Tm13	31.1	17.1	6.1	0.93
2021/04/01 - 2022/03/01	All	Tm15	30.8	18.2	5.5	0.92
2021/04/01 - 2022/03/01	West	Tm13	37.4	21.7	5.2	0.93
2021/04/01 - 2022/03/01	West	Tm15	36.1	22.9	4.4	0.92

The thermal behavior of the west facing panels has been investigated using a similar method compared to the east facing panels. Figure 12 depicts the median heat loss coefficients of the different west facing panels as a function of the wind speeds, separated by dataset and wind direction. The different types of heat loss coefficients (total heat loss coefficient U, independent heat loss coefficient U_c and the wind dependent heat loss coefficient U_v belonging to these plots can be found in Table 4. Panel 17 stands out as it shows a relative high heat loss coefficient. Panel 13 en 15 show very similar behavior. When we compare the datasets with the wind direction from the west with the full datasets with unfiltered wind direction it can be seen that the independent heat loss coefficient increases a bit unlike the wind dependent U_v value. Panel 15 and 16 are very suitable to directly compare the behavior of west and east facing panels, as they are located directly opposite towards each-other. The U-value of the west facing panel increases more, compared to the east facing panel, when we filter on



wind-direction from the west. Wind cooling is more affective when the front side of the panel faces the wind directly.

3.1.2.2 Land versus floating modules

In Figure 13: Schematic drawing of the location of the panels of which the temperature has been measured of the FPV system (left and the land system (right) a drawing of the location of the panels of which the temperature has been measured for both the FPV and the land based system can be found. Taking into account the data availability of the different sensors, we can conclude that a comparison between land based and FPV panels can be made best when the panels 30 and 10 (East facing), 39 and 9 (West facing) and 27 and 7 (West facing)

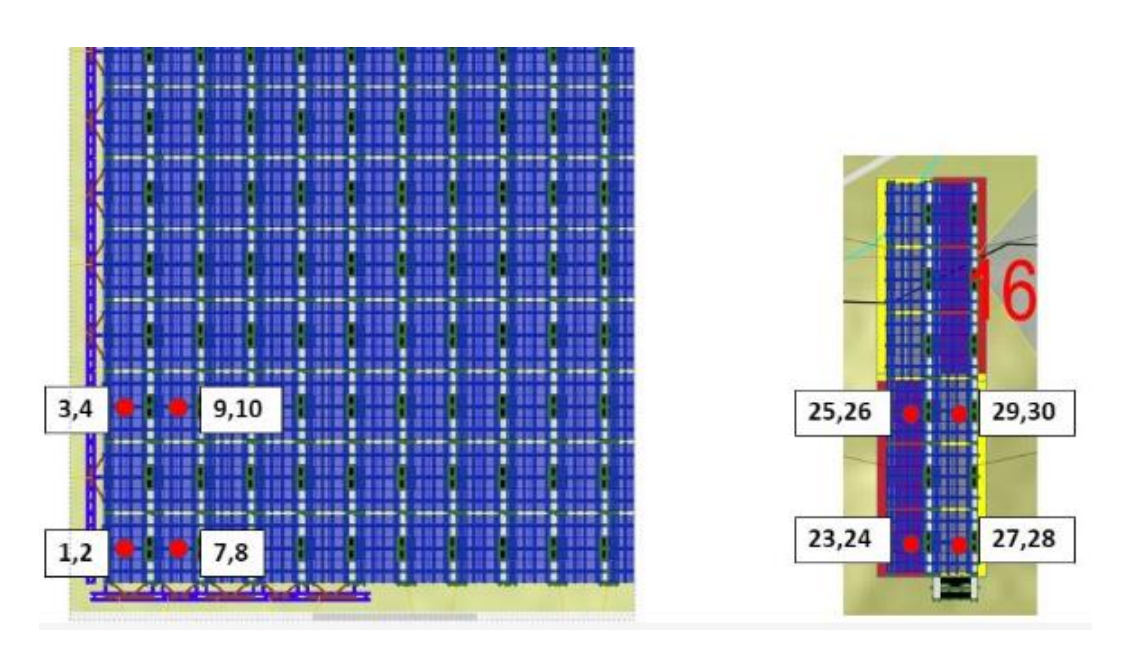


Figure 13: Schematic drawing of the location of the panels of which the temperature has been measured of the FPV system (left and the land system (right)

In Table 5Table 4 the irradiance weighted average temperatures of the floating and the corresponding land based panels can be found. The land based temperatures are between 1.1 degree and 2.4 degree warmer in this period.

Table 5: Irradiance weighted temperatures of land and floating PV panels. All wind directions and wind direction filtered from west

Location panel	Wind direction	Panel	Orientation	IWAT [°C]	Delta T (Land - Floating) [°C]
Land	All	30	East	30.0	1.1
Water	All	10	East	28.9	
Land	All	29	West	29.7	1.7
Water	All	9	West	28.0	
Land	All	27	West	29.3	1.9
Water	All	7	West	27.4	
Land	West	30	East	29.0	1.7
Water	West	10	East	27.3	
Land	West	29	West	28.1	2.4
Water	West	9	West	25.7	
Land	West	27	West	27.0	2.2
Water	West	7	West	24.8	

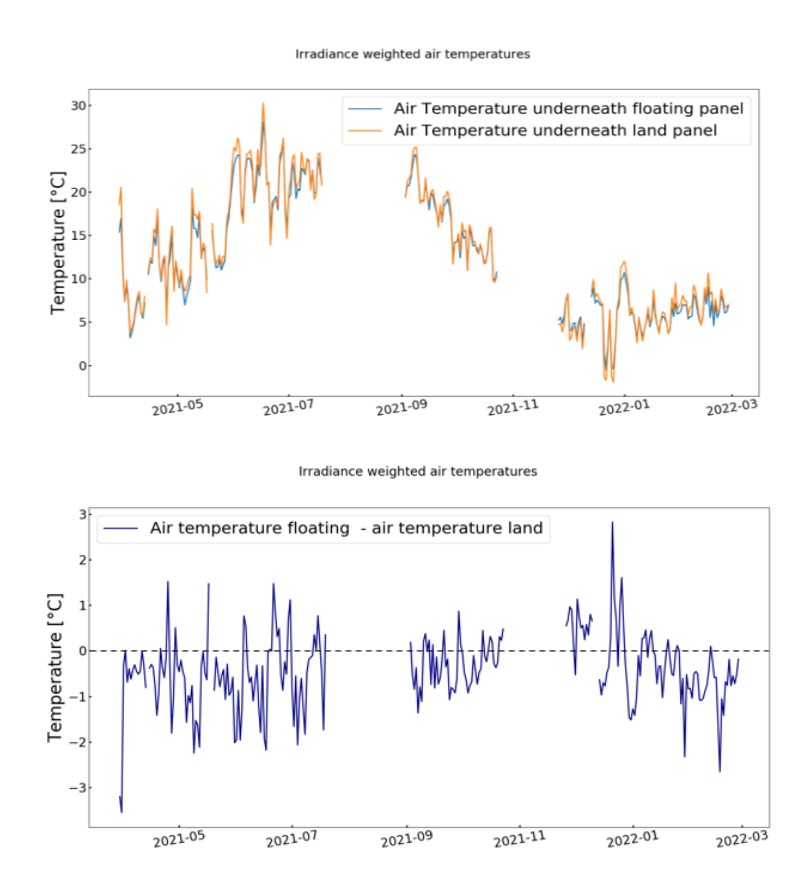


Figure 14: Irradiance weighted air temperature underneath floating and land based panels (top). Difference in air temperature underneath the PV panels (below)

The air temperature underneath the PV module can play a large role in the cooling effect of FPV. In Figure 14 (top) the irradiance weighted air temperature beneath a floating panel and a lased based panel are depicted. The difference in temperature is plotted in the bottom graph. The air temperature behind the FPV panel is a bit lower roughly between spring and fall. In the winter months, the air temperature behind the FPV panel is higher compared to the air temperature behind the land based panel.

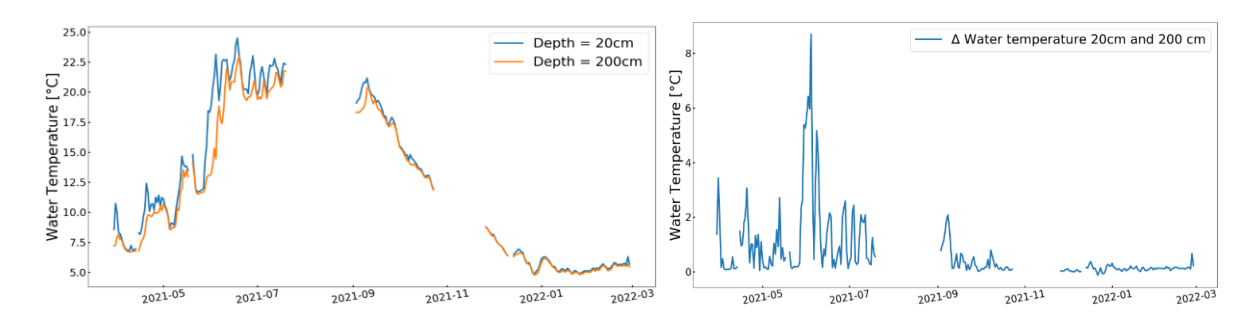


Figure 15: Irradiance weighted daily water temperature measured at a depth of 20cm and 200cm (left). The right figure shows the difference in these temperature (T depth 20cm - T depth 200cm)

The water temperature might influence the air temperature on the rear side of the PV panel. Irradiance weighted water temperatures are determined over the measurement campaign. The



temperature varies between ~5°C in winter and ~23°C in summer. When we measure the temperature of the water at different depths, we observe stratification already in the first 200cm of water depth (up to 8°C in the summer). Only the water surface interacts with the air in terms of heat-exchange.

To scan to what extent different parameters influence the difference in panel temperature between land and floating PV panels, linear fits have been made. The difference in panel temperature (ΔT land – water) has been plotted as a function of: plain-of-array irradiance, ambient temperature, water temperature (dept 20cm), wind speed and finally the difference in air temperature behind the PV panels (temperature (ΔT air land – floating). In Figure 16 these scatterplots with the corresponding linear fits can be found for both the comparison between the panels 29 and 9 (facing West) and panels 30 and 10 (facing East). The strongest relation is observed between the difference in panel temperature (ΔT land – water) and the difference in air temperature behind the PV panels (ΔT air land – floating).

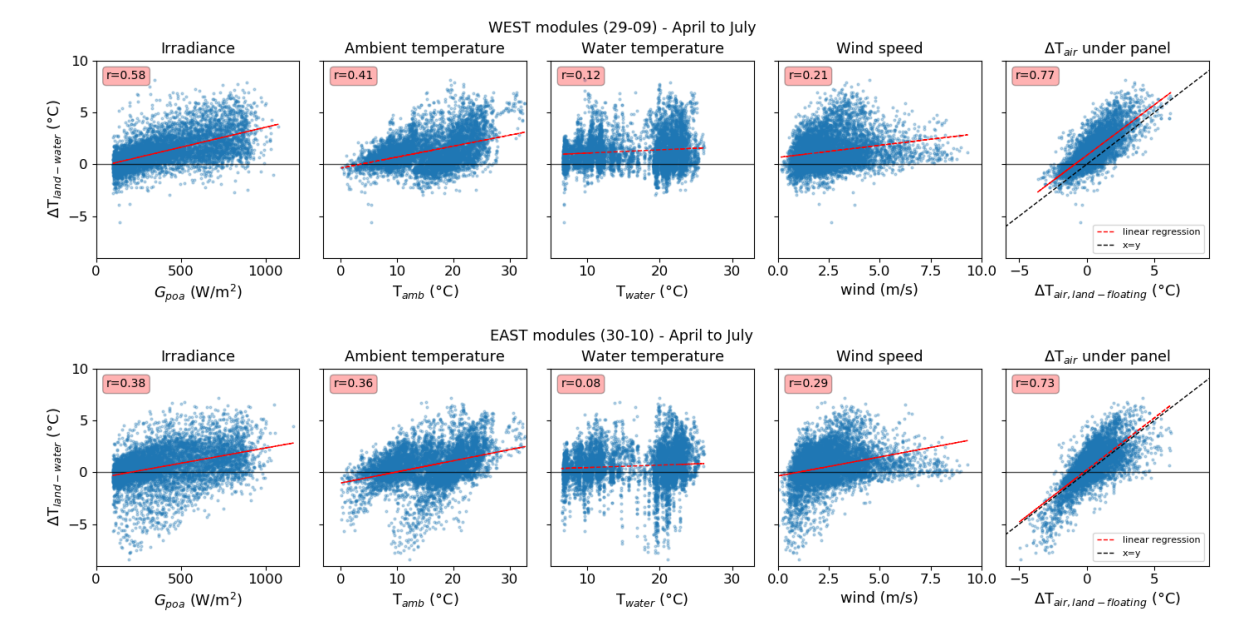


Figure 16: Scatter plots showing if the module temperature difference between land and floating modules can be correlated to the parameters: irradiance, Tamb, Twater, wind speed and DT air underneath modules between land and floating. Top row: west modules (29 land, 09 floating); bottom row: east modules (30 land, 10 floating).

Figure 17 shows a similar scatterplot (also with the panels 27 and 7), the temperature difference between land and floating PV panels is directly proportional to the difference in air temperature at the rear of the PV panel. The color coding represents the temperature of the water. It can be seen that the absolute value of the water temperature shows a limited relation with the differences in panel temperature.

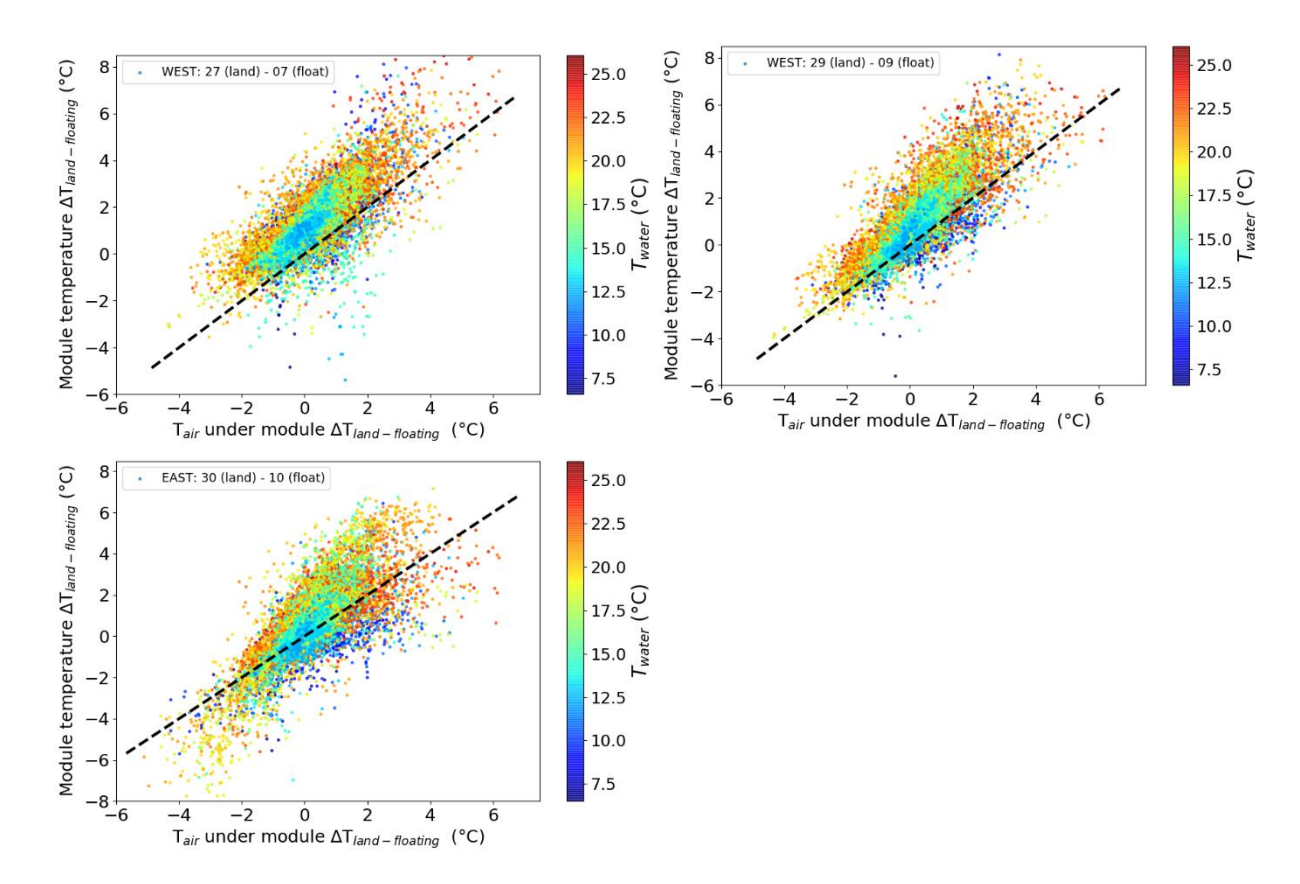


Figure 17: Scatter plot showing that the temperature difference between land and floating modules is directly proportional to the ΔT between the air temperature recorded underneath the land and floating modules. On the y-axis, ΔT >0 indicates than land modules has higher T than water module. The color bar shows water temperature, while the dashed line indicate the linear correction x=y. Measurement period: 1-04-2021 to 24-10-2021.

3.2 Yield model adapted for FPV module temperatures

In order to define which are the parameters that mostly influence the module temperature, at first we evaluated the correlation between the measured T_{module} of a floating module with the measured environmental parameters: irradiance (G_{poa}) , ambient temperature (T_a) , water temperature (T_w) and wind speed (v). To do this, we plotted the module temperature versus each of the parameter, for the whole measured period, as shown in the scatter plots of Figure 18. Additionally, we calculated the Pearson coefficients "r", as reported in the red box in each plot. The Pearson correlation coefficient ("r") measures the strength of the linear relationship between two variables. It has a value between 1 to 1, with a value of -1 meaning a total negative linear correlation, 0 being no correlation, and + 1 meaning a total positive correlation. It can be seen that G_{poa} , T_{amb} and T_w all have high "r" values (above 0.73), meaning strong (positive) correlation; on the other hand, wind speed only shows a value of around -0.3, meaning a moderate (negative) linear correlation.



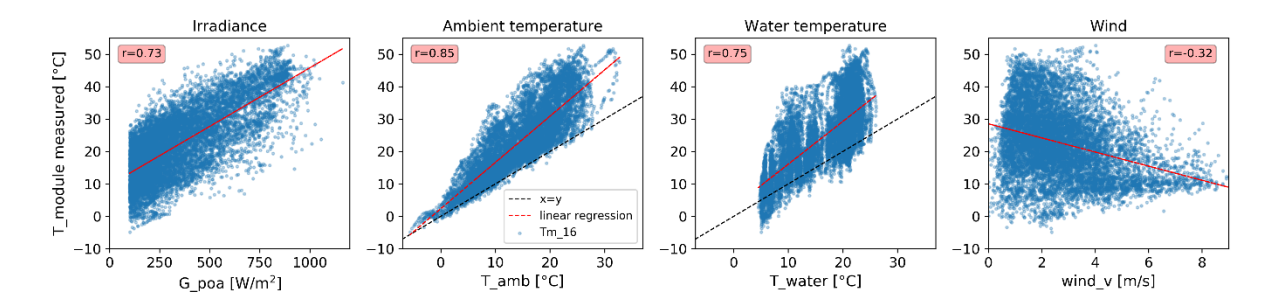


Figure 18: Scatter plots showing dependence of module temperature on the main environmental parameters: plane-of-array irradiance, ambient temperature, water temperature and wind speed. In the red boxes, the Pearson correlation coefficients are reported.

It should be noticed that the environmental parameters are also correlated between each other to a certain extent. Table 6 shows the correlation matrix between all parameters. As expect, ambient and water temperature are strongly correlated (r=0.89). Additionally, it can be observed that the water temperature is more strongly affected by the wind speed (r=-0.43), than ambient temperature is (r=-0.27). The data set considered includes all values resampled every 10-min with a filter on irradiance G_{poa} >100 W/ m^2 .

Table 6: Correlation matrix (Pearson coefficients) between all environmental parameters and T_{module}.

	T _{module}	G _{poa}	T _{amb}	T _{water}	v (wind speed)
T _{module}	1	-	-	-	-
G _{poa}	0.73	1	-	-	-
T _{amb}	0.85	0.35	1	-	-
T _w	0.75	0.25	0.89	1	-
v (wind speed)	-0.32	-0.10	-0.27	-0.43	1

This preliminary analysis on the correlation coefficients justifies the choice of modelling the floating module temperature as a function of all the aforementioned parameters: plane-of-array irradiance, ambient temperature, water temperature and wind

$$T_{module} = f(G_{poa}, T_a, T_w, v).$$

3.2.1 Model build-up

We use regression analysis-based implicit correlations for estimating the module temperature of the floating panels. The correlations have been derived from the energy conservation approach, according to which E_{in} = E_{out} . The steady state heat transfer equation for floating PV modules (for a unit module area) can be rewritten as:

$$G_{poa}(1-\eta) = c_1 * (T_m - T_a) + c_3 * v * (T_m - T_a) + c_7 * (T_m - T_w),$$

where the module conversion efficiency η is considered T-dependent, such that

 $\eta = \eta_{STC}(1 + \gamma(T_m - T_{STC}))$, where γ is the power temperature coefficient, η_{STC} is the efficiency at standard test conditions (STC), T_{STC} =25°C is the STC temperature, and T_m is the instantaneous module temperature.

The coefficients c_1 , c_3 and c_7 are found with a python-based linear regression model in which the fit is done using the least squares approach. In particular, we used the weighted least squares ("wls") regression model, with the aim of giving more weight to observations with high values of G_{poa} . We



thus use the weighted linear regression method where the weight is an increasing function of G_{poa} , that we chose to be the square function, i.e. G_{poa}^2 .

From a physical point of view, the coefficients c_1 and c_3 represent the constant and wind-dependent parts of the heat loss coefficients (or U-value, $U = U_c + U_v v [W/m^2K]$), while c_7 represents the heat loss coefficient between module and water (thus, accounting for the heat exchange on the rear side of the module). However, it should be noticed that, in our floating system, the rear side of the modules is not directly in contact with the water. In general, higher values of heat loss coefficients mean better cooling capacity (easier for the module to dissipate its thermal energy).

Once the coefficients are found, the heat balance equation can be rewritten to calculate the modelled module temperature, as:

$$T_{m} = \frac{T_{a}(c_{1} + c_{3}v) + c_{7}T_{w} + G_{poa}(1 - \eta_{STC}(1 - \gamma T_{STC}))}{c_{1} + c_{3}v + c_{7} + G_{poa}\eta_{STC}\gamma}$$

3.2.2 Model validation

To verify the accuracy of the model, we used the statistical indices: coefficient of determination (R²), root mean square error (RMSE) and mean absolute error (MAE), defined as:

$$R^{2} = \frac{\left[\sum_{i=1}^{n} (P_{i} - P_{mean}) (O_{i} - O_{mean})\right]^{2}}{\sum_{i=1}^{n} (P_{i} - P_{mean})^{2} \sum_{i=1}^{n} (O_{i} - O_{mean})^{2}}$$

$$RMSE = \sqrt{\frac{\sum_{i=1}^{n} (P_{i} - O_{i})^{2}}{n}}$$

$$MAE = \left|\frac{\sum_{i=1}^{n} (P_{i} - O_{i})}{n}\right|$$

Where P_i and O_i are the predicted and observed values, respectively (i.e. simulated and measured T_{module}). The subscript mean indicates the mean value of the variable, and the letter n indicates the number of values. In the model we use the following general assumptions and filtering conditions (Table 7).

Table 7: General assumptions and filtering conditions used for the regression model.

Albedo	0.08
G _{poa}	Modelled with pylib starting from measured GHI
Reduced wind speed	wind_ $v_{red} = wind_v^*(h_{PV mod}/h_{ wind sensor})^{0.2}$ where h=height
Wind speed filter	0 < v < 6 m/s
Irradiance (Gpoa) filter	100 < G _{poa} < 1300 W/m ²
Time period	01-04-2021 to 02-03-2022
Resampling	10-min
Regression model	Python WLS (Weighted Least Squares) with weight: Gpoa ²
Coefficients	C ₁ , C ₃ , C ₇

In the selected time period (longest period with sufficient number of temperature sensors still in operation), we could validate the model using 2 west-oriented modules (13 and 15) and 3 east-



oriented (12, 16 and 20). The regression model yielded the following coefficients and statistical indices, as shown in Table 8.

Table 8: Results of the regression model	for 5 modules, in terms of co	efficients, number of data	apoints and statistical indices.

	West-oriented		East-oriented		
	M_W_13	M_W_15	M_E_12	M_E_16	M_E_20
C 1	19,2	21,9	22,5	24,1	23,7
C ₃	5,4	4,8	5,1	5,1	3,9
C ₇	2,4	0,5	1,2	-0,5	-1,6
#rec	10215	10209	10078	10077	10064
MAE	1,57	1,56	1,45	1,35	1,70
RMSE	2,14	2,09	1,97	1,85	2,19
R ²	0,960	0,964	0,963	0,966	0,969

It can observed that the coefficient c_7 , accounting for the water temperature, varies from slightly positive (up to 2.4, for module 13) to slightly negative values (up to -1.6, for module 20). This seems to indicate that the water does not have a strong cooling effect on the floating panels, at least for this specific test site with this specific weather conditions. It should be recalled that in this installation, the water is not in direct contact with the module surface. Additionally, it is interesting to notice that, in the monitored period, the measured water temperature was for approximately half the time higher and half the time lower than the ambient temperature. This is shown in the histogram in Figure 19. If, in the regression model, we would only consider datapoints where $T_{amb} > T_w$, then c_7 would increase, while c_1 would decrease proportionally. On the other hand, if considering only datapoints where $T_{amb} < T_w$, the opposite would take place: strong decrease of c_7 and strong increase of c_1 , as shown in the plot on the right-hand side of Figure 19. We also tried to run the regression model without considering c_7 at all (thus, without accounting for the water temperature), and the only consequence was the re-adjustment of the coefficient c_1 , such that the sum of the two coefficient (c_1+c_7) remains approximately the same.

The results presented in the rest of the report refer to the situation in which we consider all three coefficients (c_1 , c_3 and c_7) without applying any filtering condition based on the relationship between T_{amb} and T_w .

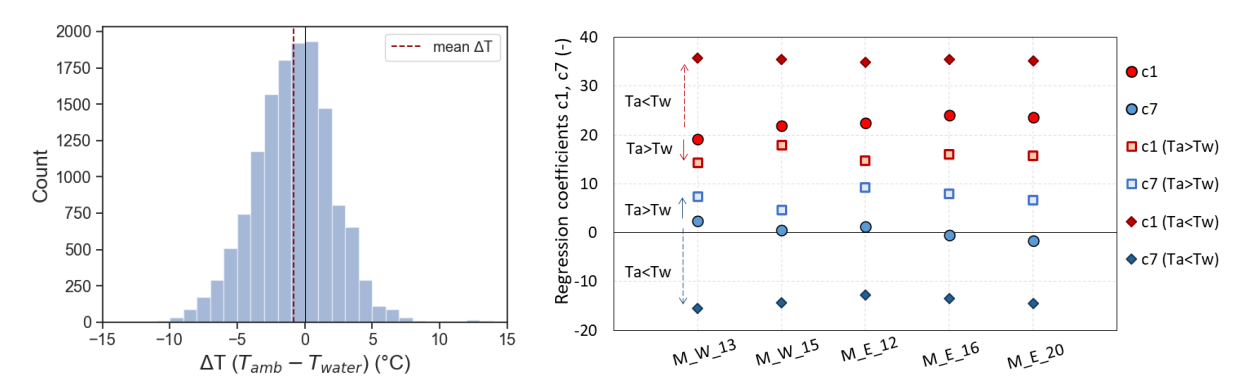


Figure 19: Left: Histogram showing temperature difference between ambient and water temperature (@20 cm underwater). Right: variation of coefficients c1 and c7 at varying dataset (no filter, $T_{amb} > T_w$, $T_{amb} < T_w$).

Scatter plots of measured and simulated values of T_{module} for all modules are shown in Figure 20. The dashed black line represents the x=y line, where predicted values equal the measured ones. The color bar represents the wind speed. In general, it can be seen that the wind speed does not present a strong correlation with the model accuracy and with temperature variations; this was expected, since a relatively low correlation coefficient was found between wind speed and T_{module} (see Table 6).



Overall, the scatter plots show that the model provides a good fit between predicted and measured values. As reported in Table 8, the R^2 value is around 0.96-0.97, while the mean absolute error is around 1.4-1.7 °C.

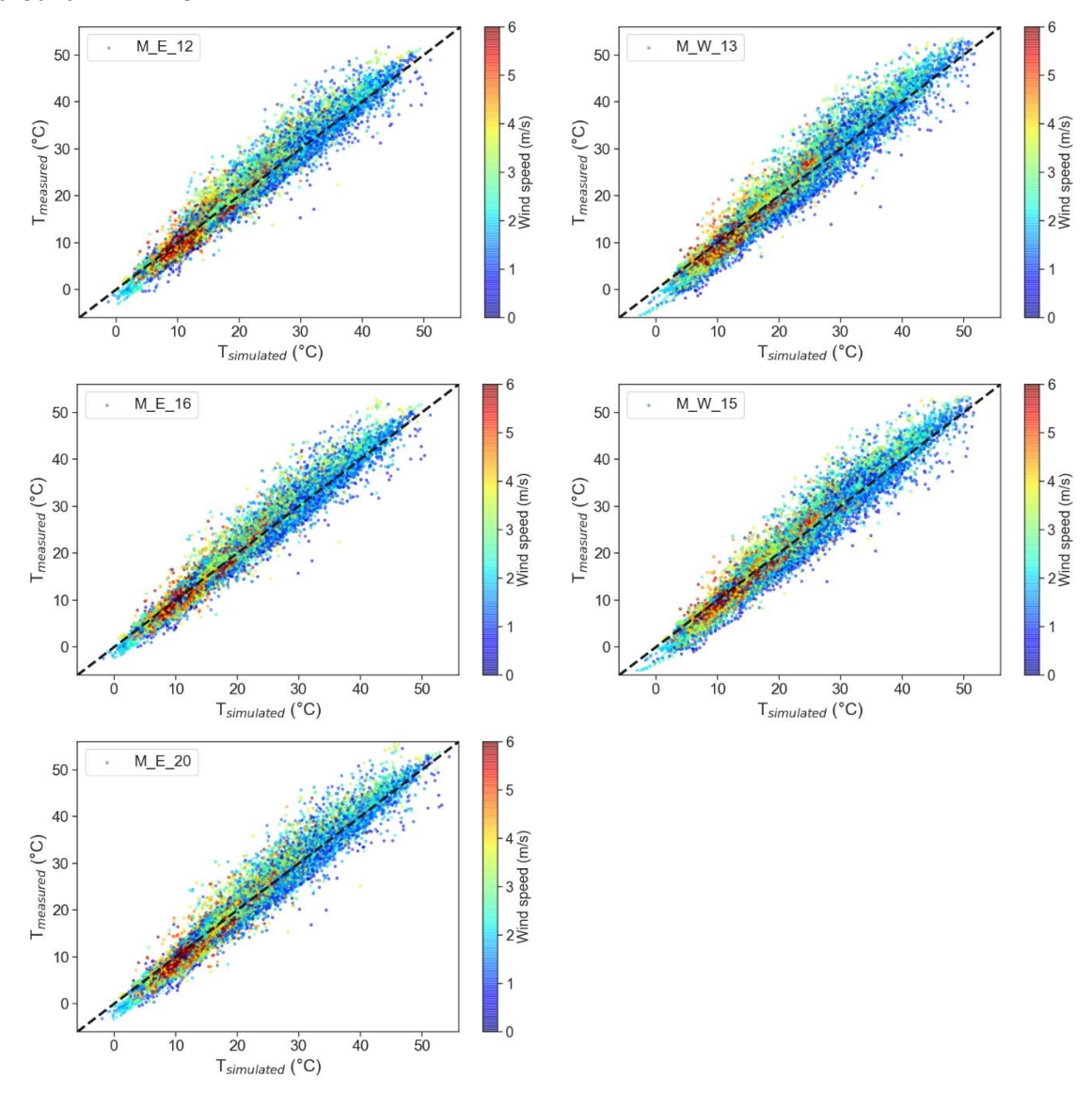


Figure 20: Scatter plots showing the comparison between measured and simulated T_{module} for all the considered modules, as a function of wind speed (color bar).

Figure 21 shows the comparison between the modelled and measured T_{module} , for a representative module (M_16), on a timescale including the whole examined period (April 2021 to March 2022, with data gaps in July and November).



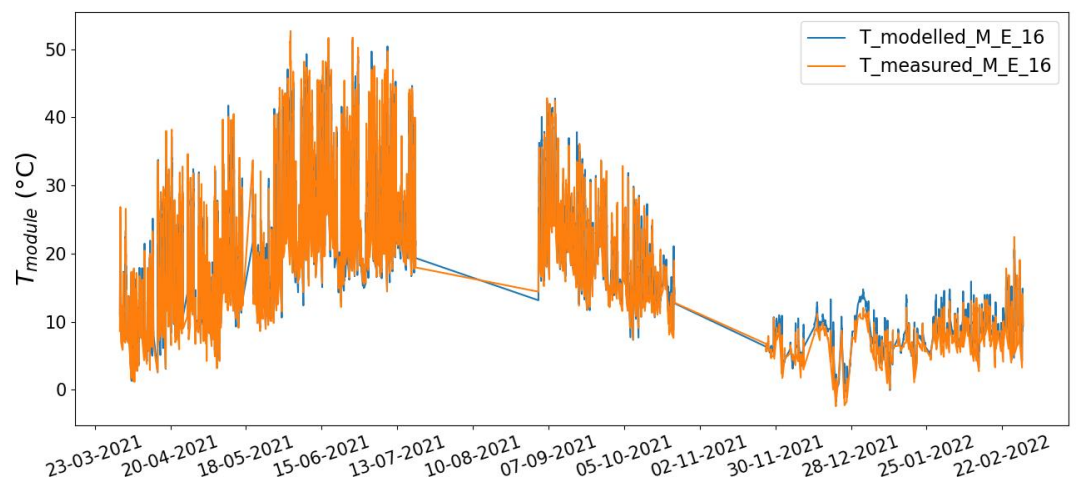


Figure 21: Timeseries of both simulated and measured T_{module} for module M_16 (whole period: 1-04-2021 to 2-03-2022).

In Figure 22 (east module, M_16) and Figure 23 (west module, M_15) we zoom-in over a 5-day period in September, where the daily temperature profiles can be better observed. In the bottom part of the plots, the temperature difference DT between the simulated and measured T_{module} is shown.

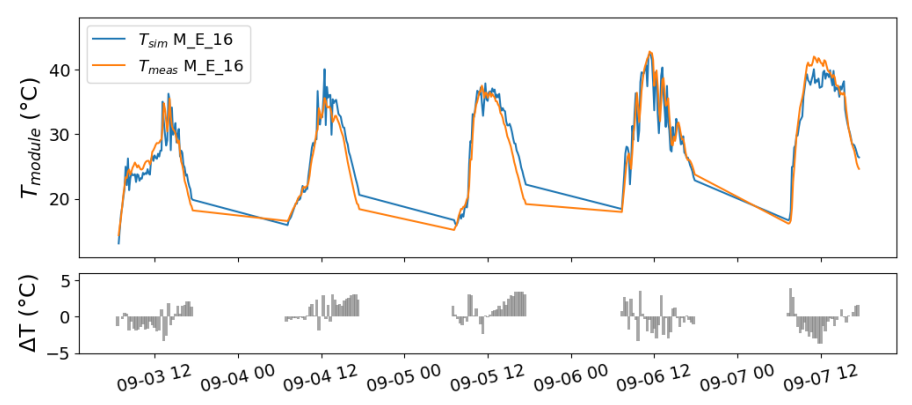


Figure 22: Top: timeseries over a 5-day period (3/7-09-2021) showing simulated and measured T_{module} of east-oriented module $M_{-}16$. Bottom: temperature difference DT between T_{sim} and T_{meas} .

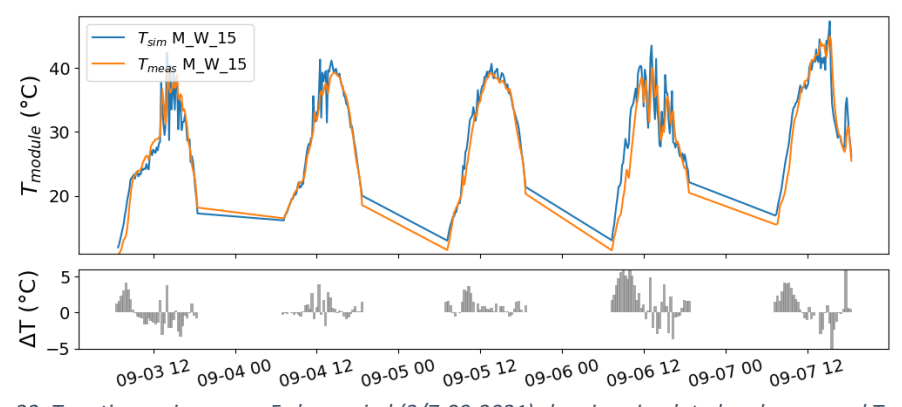


Figure 23: Top: timeseries over a 5-day period (3/7-09-2021) showing simulated and measured T_{module} of west-oriented module $M_{\perp}15$. Bottom: temperature difference DT between T_{sim} and T_{meas} .

The comparison over the full period can also be done in terms of daily irradiance-weighted-average temperature, as shown in Figure 24 and Figure 25, showing the east- and west-oriented cases. It can be observed that in the spring and summer seasons the model seems to underestimate the module temperature, while in winter it mostly overestimates it. On a daily basis, the DT between the modelled and simulated T_{module} mostly lies between ±2.5°C. When considering all 10-min datapoints, the box



plot of Figure 26 shows that, ignoring the outliers, most DT values range from approximately -2.5 to +5°C.

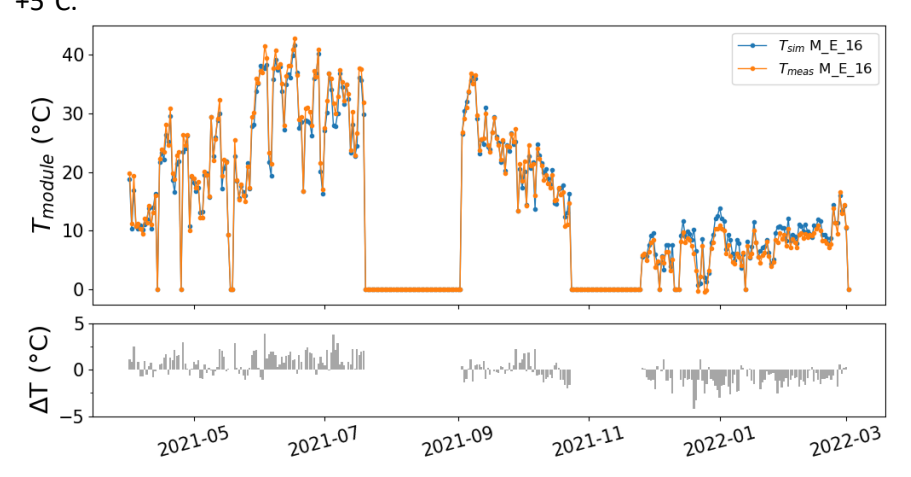


Figure 24: Daily irradiance-weighted-average temperature (top) and DT (bottom) between T_{sim} and T_{meas} for module M_16.

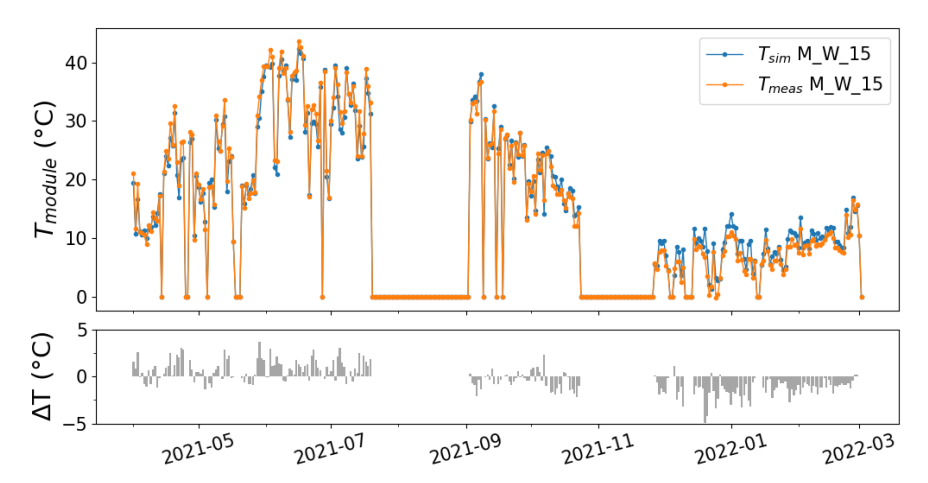


Figure 25: Daily irradiance-weighted-average temperature (top) and DT (bottom) between T_{sim} and T_{meas} for module M_15.

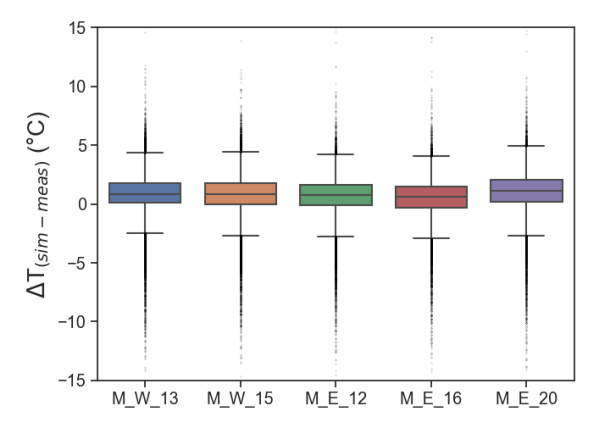


Figure 26: Boxplot showing DT between T_{sim} and T_{meas} for all modules (10-min datapoints).

3.2.3 Modelling results

We use the model to investigate further the cooling effect of the water on the module temperature. In particular, we carry out two investigations:

- Comparison between floating and land system;



- Temperature gradient within the floating system (temperature difference between modules at different locations within the large scale FPV system, i.e. edge effects, etc.).

Figure 27 shows the results, in terms of (heat loss) coefficients, for the floating versus land analysis. A distinction is made between west and east orientation. At first, we include in the model all coefficients c_1 , c_3 and c_7 , for both modules in the land and on the floating system. We would have expected for the land modules a value of c_7 close to zero (i.e. no correlation with water temperature), but negative values of -2.4 and -5.2 are obtained for the west and east case respectively (Figure 27b). As we saw earlier, this affects the c_1 coefficient too (the lower the c_7 , the highest the c_1 , to compensate).

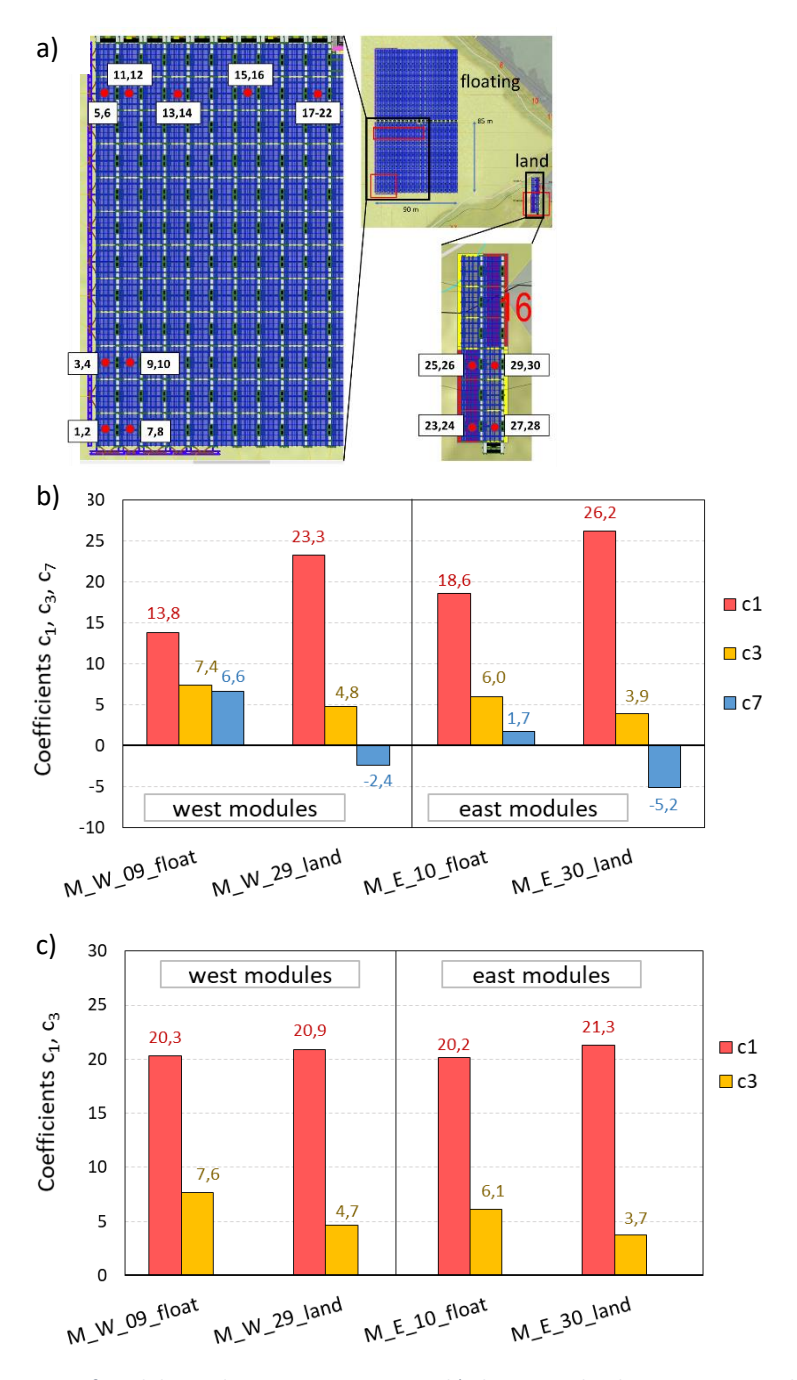


Figure 27. a) Overview of modules and temperature sensors. b) Floating vs land comparison results in terms of coefficients, distinguishing for east and west oriented modules. All coefficients (c_1 , c_3 , c_7) included in the model. c) Only coefficient c_1 and c_3 included in the model.



When we exclude c_7 from the model, we obtain the results shown in Figure 27c. As expected, the resulting c1 coefficient now is approximately equal to the sum of c_1 and c_7 as calculated earlier (Figure 27b). It can be seen that now the c_1 coefficients of the land and floating modules are almost the same (or even slightly higher for the land module, contrary to what it would be expected). On the other hand, we can see that the wind-dependent part of the heat-loss coefficient, i.e. c_3 , (which remains rather constant when including or excluding c_7 from the equation) is higher for the floating module than for the land module. This is the case for both the east and west configuration. This means that overall, when the coefficients are all summed up, the floating system shows a slightly better cooling capacity, mainly attributed to the effect of the wind. The difference is however very small.

When it comes to the analysis of the temperature gradient within the floating system based on the different location of the modules, we apply a similar approach: we analyze the coefficients (both including and excluding c₇, Figure 28a and Figure 28b, respectively) and distinguish between the west and east orientation.

As previously mentioned, a number of sensors got damaged during the measurement campaign and became unreliable, thus for the west-orientation case we could use only three sensors (13, 15 and 17) and for the east-orientation case we used four (6, 12, 16, 20). The exact location of those sensors can be found in the schematic reported in Figure 27a. The higher the sensor's (identification) number the more the module is located towards the internal side of the floating system (i.e., M_E_06 is the most external, close to the edge, while M E 20 is the most internal module).

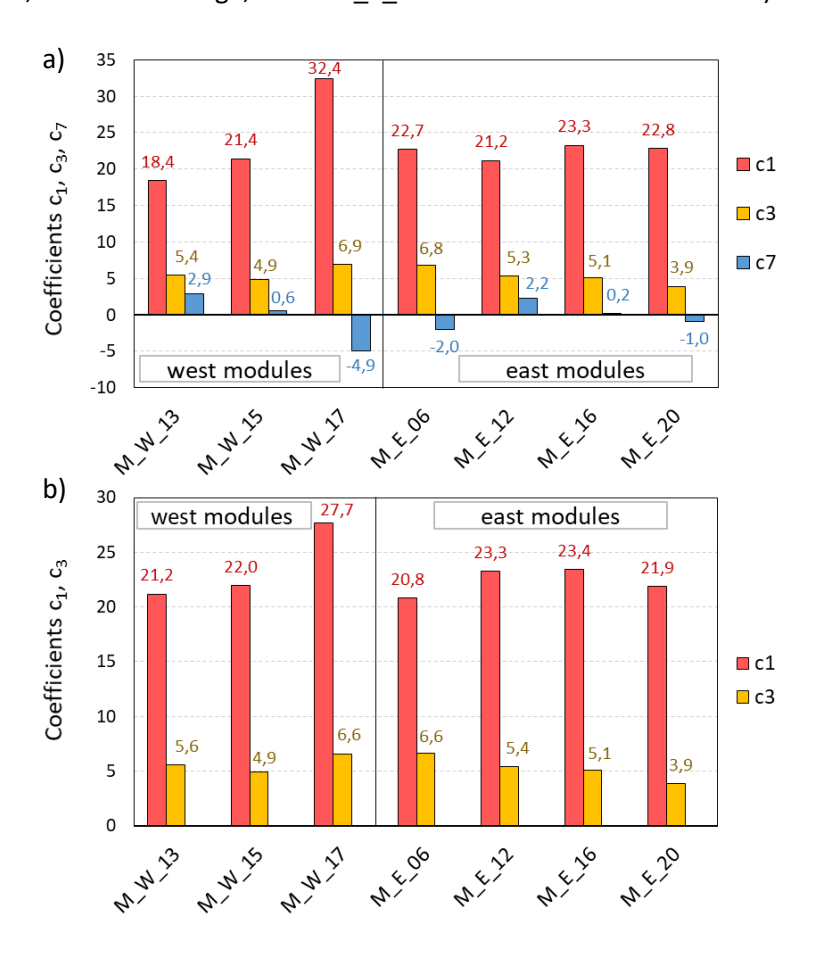


Figure 28. Analysis of temperature gradient based on different module location within the floating system a) Results in terms of coefficients, distinguishing for east and west oriented modules. All coefficients (c_1 , c_3 , c_7) included in the model. c) Only coefficient c_1 and c_3 included in the model.



The analysis of the modelling results are not so straightforward. When looking at the water-dependent coefficient c_7 (Figure 28a) no trend can be identified. Excluding the c_7 coefficient from the analysis, we obtain the results shown in Figure 28b. Also in this case, when looking at the constant heat-loss coefficient c_1 is it not possible to identify clear trends.

On the other hand, the wind-dependent coefficient c_3 does show a trend, especially clear when observing the east-facing modules comparison. c_3 is the highest for the modules closer to the edges and progressively diminishes when going towards the inner side of the system. This result is in line with expectations, as modules at the edges of the system are more exposed to the open air. For the west oriented modules, c_3 reduces from module 13 to module 15, but module 17 shows again an unexpected higher value.

All in all, no strong conclusions can be drawn from the modelling results, mainly because the measurement results themselves did not show the temperature differences and gradients initially expected, and partly because the model itself can still present some inaccuracies.



4 Irradiance modelling

4.1 Introduction

In order to further develop and validate the BIGEYE irradiation module for solar parks, the geometry and gathered field data of a land-based solar park near Oosterwolde is used. In the test field, at a a number of locations, irradiation sensors facing up and facing down were placed under a row of module tables in order to measure the irradiation penetration and the back side illumination of the PV modules. These measurements were further used to validate the simulations.

4.2 Approach

The ground irradiance data is modelled by adapting TNO's propriety software package BIGEYE that was originally developed to calculate the annual yield for bifacial solar parks. Nowadays it is widely used in TNO research projects, ranging from combined PV-agricultural farms to vehicle-integrated PV.

Using BIGEYE, we built a model of the test field setup with the available data from data sheets, project partners and measurements taken on-site. We aim to give insight in the amount of sunlight that reaches the ground below and the rear of the solar panels. We also determine what irradiation contributions (such as reflections or transparancy) to add and which contributions to ignore to get an accurate model without too much requirements on computing power and time. To finish, we compare the data from the simulations of the final model with actual measurements.

The model parameters are strongly affecting the output in terms of simulation duration (computation time needed) and quality of the data. For example, increasing the resolution of the model results in better representation of the measured data by the model, while leading to longer simulation durations. A similar effect is also observed when the simulated layout is changed. Depending on the size of the modelled tables, simulations might take up to 5h. Nevertheless, high resolution is required, along with other parameters such as albedo, specular reflection and back-sheet reflection, in order to obtain proper results that are comparable to measured data. The effects of the parameters are discussed in the next section. We performed the simulations using meteorological data collected by Royal Netherlands Meteorological Institute (KNMI). In our simulations², we improved the model by comparing simulations results with the data for 8 September 2021. The updated model has been validated against observations taken on 17 July 2021 data.

Prior to moving towards the model validation, it is essential to know the positions of the sensors. In Figure 29, a schematic representation of the positions of the sensors are given; the figure is not proportional to the actual measurements.

-

² For sake of completeness: the simulations were run using 400 number of points on hemi-sphere for sky dome discretisation and 0.1 m ground mesh size



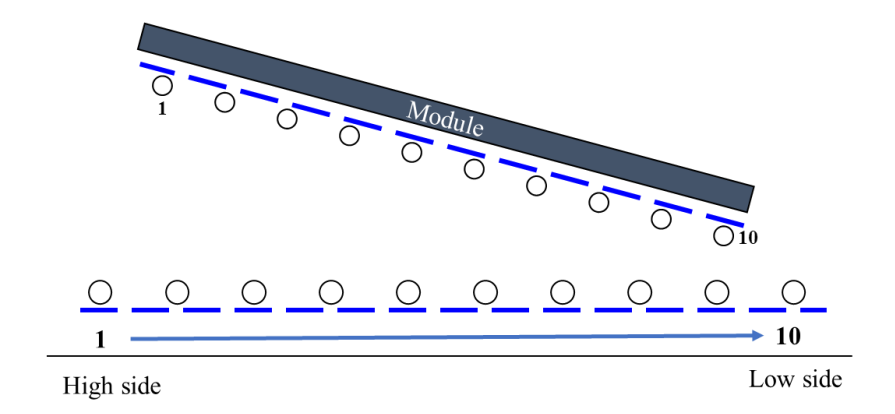


Figure 29. Schematic representation of the sensor positions in the test field. It should be noted that the image is not proportional to the real test field. Sensors on the lower position are named "upward" looking or "ground" sensors and the ones placed underneath the module with the same angle as the module are named "downward" looking or "rear" sensors.

4.3 Model validation

We investigated the simulated irradiance on ten sensors positioned on the ground (looking upwards) and 9 sensors positioned on the rear (looking downwards) of the solar panels. The main findings showed that ground-reflected radiation (referred to as albedo from hereon), back sheet reflection, specular reflection, gap between the modules and table size were the most important parameters. Below, we briefly explain the effects of these parameters. Only representative graphs are shown in this document. The graphs of missing sensors can be supplied by TNO.

4.3.1 Albedo variation

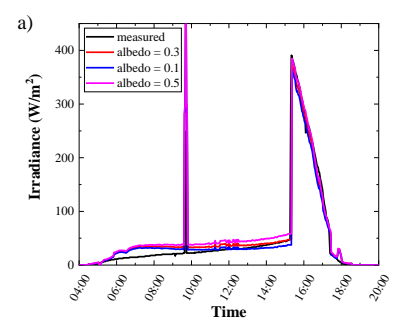
The effects of albedo were investigated by means of global and local albedo variations. In this approach, initially the albedo was set to a fixed value, meaning that the amount of reflection from the ground is identical throughout the field. Next, the albedo was locally varied from the fixed value to represent local changes in the vegetation. This hypothesis is supported by the pictures of the test field (see description of test filed) where it is clear that there is very limited vegetation at certain parts of the test field whereas grass and other plants are present at other parts.

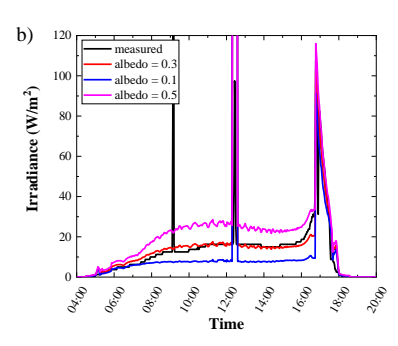
Global albedo variations

The effects of global albedo were investigated by setting the albedo to 0.1 (10%), 0.3 (30%) and 0.5 (50%). The results showed that albedo not only effects the downward looking sensors but also the upward looking sensors. The latter can be explained by secondary reflection effects, particularly when direct and diffuse light are reflected from the ground to the back of the modules. This ground reflected light, incident on the modules' back sheet is in its turn reflected by the (white) back sheet back towards the ground. In Figure 30 and Figure 31, the effects of albedo on ground and rear sensors are shown.

It can be seen from Figure 30 that the direct light (irradiance between 15:00 and 18:00) is modelled very well for all sensors irrespective of the albedo value. The irradiance from early in the morning till late afternoon (time range from 06:00 till 15:00) requires a more detailed look. It was concluded that there is no single albedo value that fits all sensors, but 0.3 represents the modelled data the best.







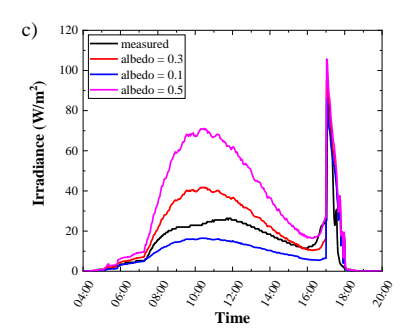
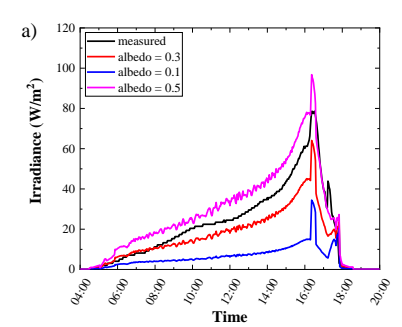
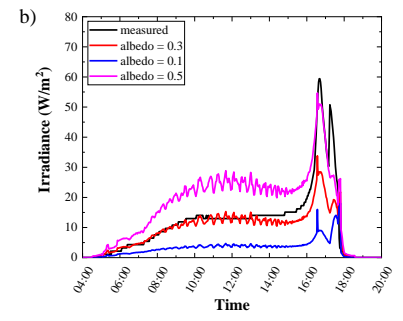


Figure 30. Effect of albedo on the modelled data for ground sensors 2 (a), 6 (b) and 8 (c). The measured data is shown with black whereas the modelled data is colour coded for each albedo value. Time scale is given as hours.

It can also be seen from the figure that the irradiance increases sharply for the modelled data around late afternoon ($^{\sim}$ 15:30) whereas a gradual increase of measured irradiance can be seen around the same time. This can be explained by the geometry of the light source. In our modelling, the light source is considered as a point source, which does not take the angular size of the sun disk into account.

Similar to ground sensors, rear sensors also show that there is no single albedo value which is good enough to represent the measured values for all sensors. It is however clear that 0.1 is underestimating the measured values, whereas 0.5 is overestimating. Therefore, it is concluded that 0.3 is the best fitting value for this test field. The observations also indicate that albedo may not be the same on all of the test field. For that reason, we also investigated the effects of locally varying albedo.





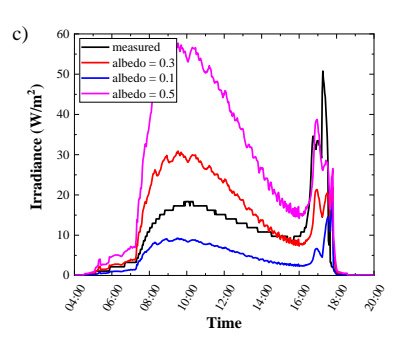


Figure 31. Effects of albedo on the modelled data for rear sensors 2 (a), 6 (b) and 8 (c). The measured data is shown with black whereas the modelled data is colour coded for each albedo value. Time scale is given as hours.

It can be seen from Figure 31 that the model is not able to represent the measured data late in the afternoon accurately. This possibly is due to effects that are not taken into account, i.e. water on the ground, reflections on shading elements like beams and frames etc., in the modelling.

Local albedo variations

The effects of local albedo variations were investigated by adjusting the model. In the model, we placed three 1 m wide dummy reflectors above the ground underneath the lower half of the table (see Figure 32). This gave us the opportunity to locally change the albedo values. The albedo of the rest of the test field was set to 0.3 based on the results discussed in the previous section.



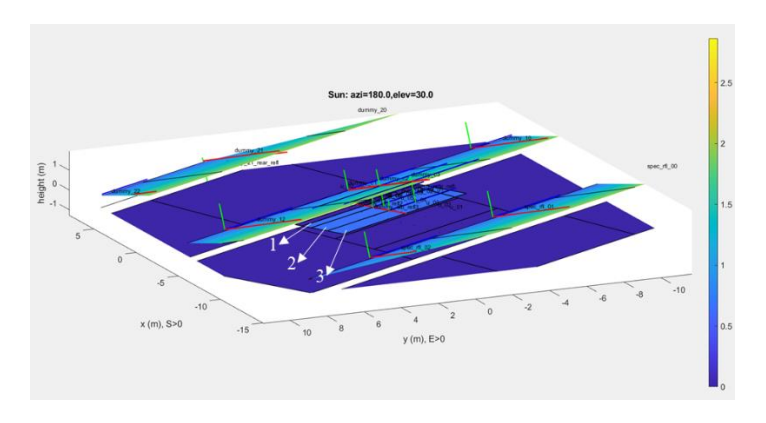


Figure 32. Schematic representation of the modelled setup. Solar panels are shown as the tilted surfaces (simulating actual system), ground is represented by a dark blue colour. Dummy reflectors are shown with light blue colour underneath the central table. They are labelled with numbers 1, 2 and 3 from the front (lower end of the table) to the back (higher end of the table).

The albedo values of these dummy reflectors were first set to 0.1 (10%). Then, they were changed to 0.05 (5%), 0.15 (15%) and 0.25 (25%) for reflectors 1 to 3, respectively. As expected, changing the albedo value locally did not have any significant effect on the simulated ground sensors 1-5 as these sensors are far from the dummy reflectors. However, it was possible to observe a decline on the modelled irradiance on sensors 6-8.

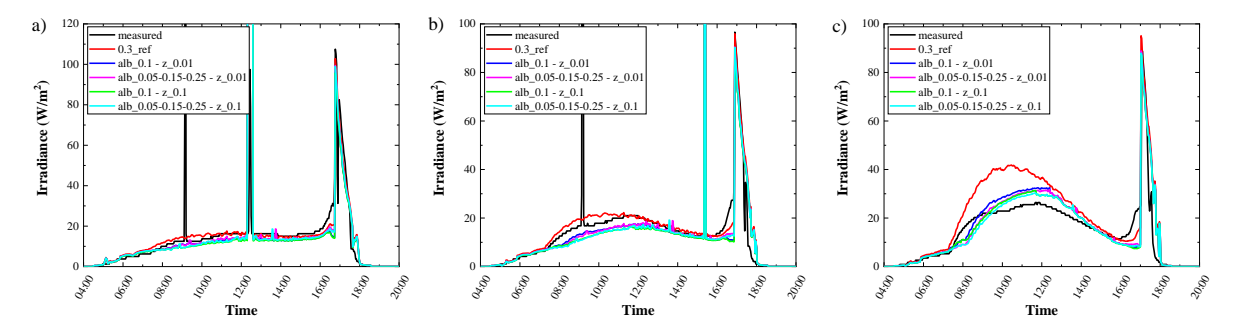


Figure 33. Effects of local albedo variation on the modelled data for ground sensors 6 (a), 7 (b) and 8 (c). The measured data is shown with black whereas the modelled data is colour coded for each albedo value. On the legend, 0.3_ref shows the modelled graph that was shown in Figure 30.c. "alb_0.1" and "alb_0.05_0.15_0.25" represent the albedo values for the dummy reflectors from 1 to 3, whereas "z_0.01" and "z_0.1" represent the height of the reflectors from the ground in m. Time scale is given as hours.

As it can be seen from the Figure 33, introducing dummy reflectors to simulate varying albedo per 1m patch results in lower modelled irradiance values. The effects are not visible when simulating the irradiance on sensors 9 (although dummy reflector 1 is underneath this sensor) and 10 as these receive a high fraction of direct light.

Since the rear sensors are affected more by albedo, we also investigated the effects on these sensors. It should be noted that the dummy reflectors cover the ground under the lower half of the PV table, up to rear sensor 5. Meaning that the albedo beneath sensors 1-4 is set to 0.3, whereas the albedo underneath sensors 5-9 varied according to the values shown in Figure 34.



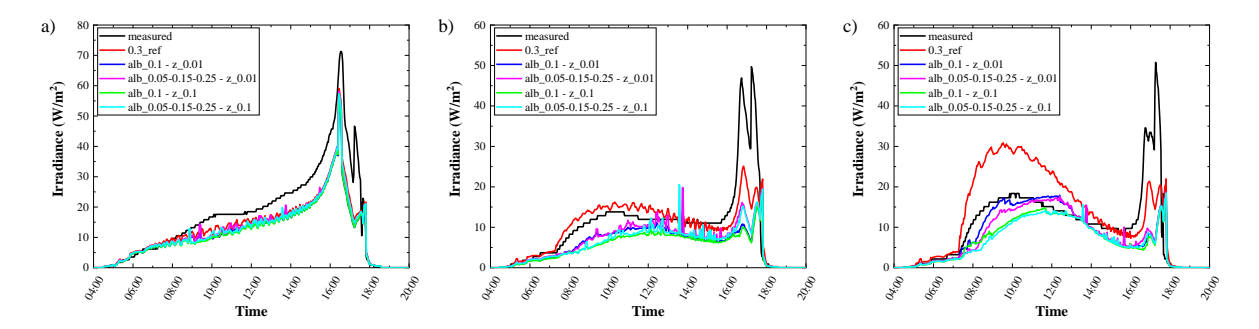


Figure 34. Effects of local albedo variation on the modelled data for rear sensors 4 (a), 7 (b) and 8 (c). The measured data is shown with black whereas the modelled data is colour coded for each albedo value. On the legend, 0.3_ref shows the modelled graph that was shown in Figure 31.c. "alb_0.1" and "alb_0.05_0.15_0.25" represent the albedo values for the dummy reflectors from 1 to 3, whereas "z_0.01" and "z_0.1" represent the height of the reflectors from the ground in m. Time scale is given as hours.

We see from Figure 34 that although sensor 4 is outside the area of dummy reflectors, the modelled irradiance on this sensor was also affected by the changes in albedo that were induced at least 0.5 m away. This effect is more pronounced when we look at sensors 7 and 8. It is clearly visible from the figures that lower albedo results in a better representation of the measured data with respect to the reference line shown in the graph. This shows that albedo variation on the ground has a strong effect on the modelled irradiances, thus it should be taken into account while designing the system.

4.3.2 Back sheet reflection

In this section, we analyse the effects of diffuse reflected light from the back sheet. In order to study the effects, we implement back sheet reflection in our model which allows us to model the additional gain (in addition to direct light) on sensors. These additional gains in irradiance can be the result of light originating from its source (direct and diffuse light) or reflected light (albedo and reflections from adjacent surfaces). To study the effect of the reflection coefficient, we set the albedo to 0.3 following earlier results and change the reflection coefficient value from 0 to 0.5 (50%) and 0.7 (70%). It was observed that changing the reflection coefficient has a clear effect on the simulated irradiance for all ground sensors (except sensor 10 which is located in the gap between two tables). As is shown in Figure 35, the effect is more pronounced as we proceed from sensor 1 (higher end of the table) towards sensor 8 (lower end of table).

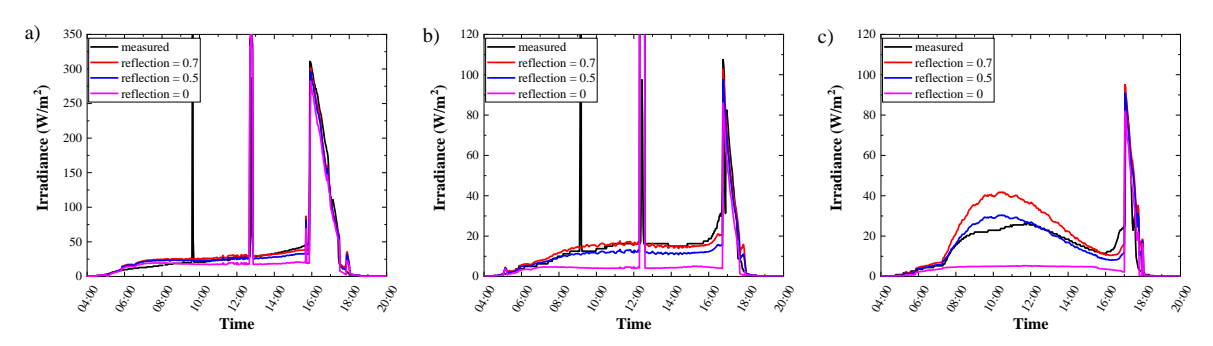


Figure 35. Effects of back sheet reflection for ground sensors 3 (a), 6 (b) and 8 (c). The measured data is shown with black whereas the modelled data is colour coded for each reflection value. The values mentioned in the graph indicates the measure of reflection (0.7 means 70% of the light is reflected from the back sheet). Time scale is given as hours.

It can be seen from the above figure that light reflected by the back sheet contributes to all ground sensor simulations and strongest on the darker sections of the PV table. It should be noted that because light intensity is reduced after each reflection, the reflection coefficient of the back sheet is



expected to have much less contribution to the simulations of the rear sensors. This is illustrated in Figure 36.

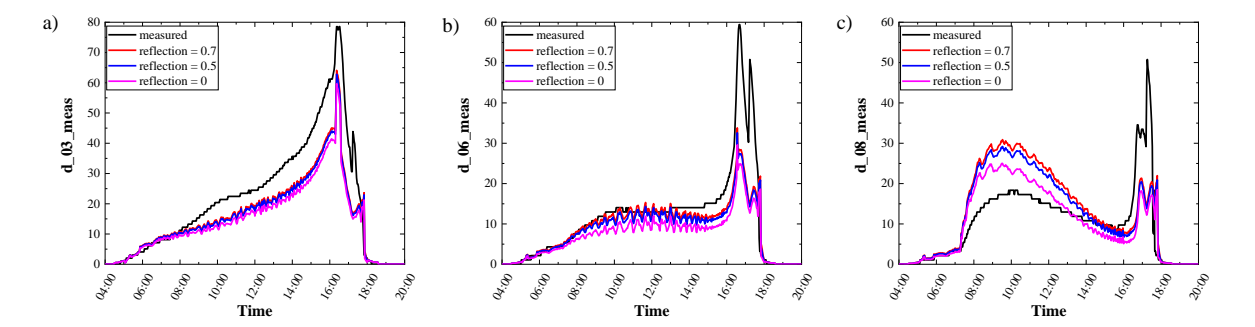


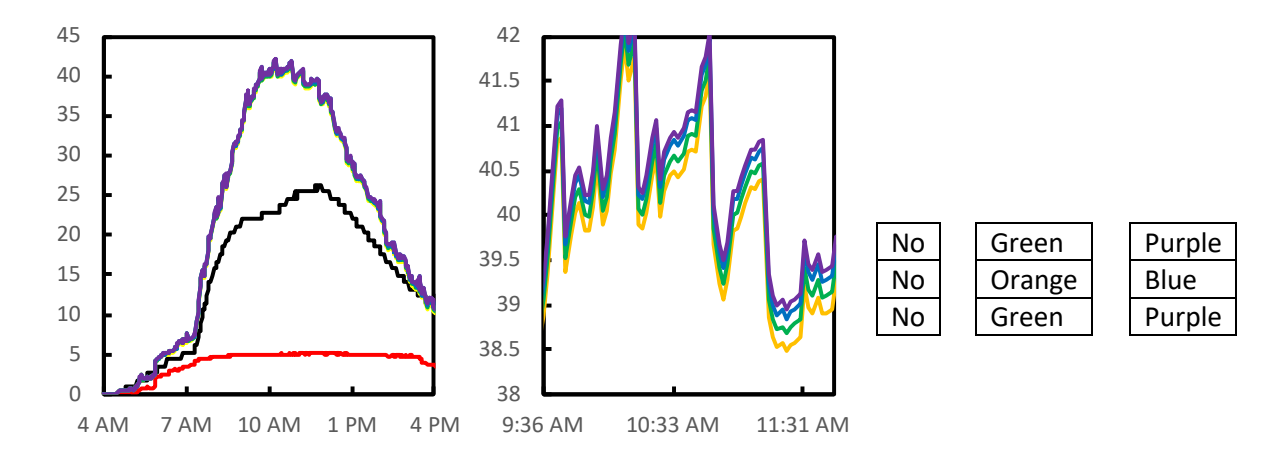
Figure 36. Effects of back sheet reflection for rear sensors 3 (a), 6 (b) and 8 (c). The measured data is shown with black whereas the modelled data is colour coded for each reflection value. The values mentioned in the graph indicate the measure of reflection (0.7 means 70% of the light is reflected from the back sheet). Time scale is given as hours.

Although high reflection coefficient values results in overestimation compared to the measured data for some of the sensors, it was concluded that 0.7 reflection coefficient is required in order to best represent all the measured data for all of the ground and rear sensors.

4.3.3 Contribution of reflections on sensors

In the previous section, we described that including the diffuse scattering of light on the rear of the solar panels, which are so-called white back sheets, improves the agreement between the observed ground irradiances and the simulated ones. However, we included diffuse reflectors behind all modules in the front and in the central row of PV panels, with each row consisting of three tables and each table 3 panels high and 10 panels wide. With a resolution of ~30 cm and a triangular grid, this means a total of 1400 grid points per table and 8400 grid points for the two rows.

Here, we investigate whether we can reduce the computing time and size of the output files by systematically adding/removing the diffuse reflector. We look at the simulated irradiance on the ground for sensor number 8. The daily profile for a number of simulations and the observations are plotted below, y-axis is the ground irradiance in W/m².



The black data is the measured data. Without the diffuse reflector in the model, red line, we clearly do not simulate the broad irradiance peak from 7 am onwards. Adding diffuse reflectors, to (a selection of) the front and central tables leads to a qualitatively good agreement between the measured data and the simulation curves, in orange, green, blue and purple. In the left graph, the differences between these curves is not visible. To elucidate the differences, a small part of the graph



is enlarged in the central picture. The overview of which coloured curve belongs to which diffuse reflectors, in the right hand panel the three rows with three PV tables is indicated, with the front row on the right hand side. The simulations never include diffuse reflectors at the rear of the back row. Diffuse reflectors were then added, first at the location labelled Orange, then Green, Blue and finally Purple. Note that each next step includes the previously added reflectors: simulation Blue has diffuse reflectors on all three tables of the central row and behind the middle table of the front row, but not behind the outside table of the front row.

In the enlargement we see that the curves are consistently higher, when we add more diffuse reflectors to the simulation. But also not the difference between one table with reflector and six tables with reflectors is about 0.5 W/m² on a total, simulated ground irradiance of 40 W/m², a mere 1.25%, much less than the differences between observations and simulations.

We conclude that it is necessary to include diffuse reflectors to mimic the optical properties of white back sheet modules. But also that we can restrict the application to an area of at most 10 m wide around the area of interest

4.3.4 Specular reflection

Based on the observed irradiance spikes on the rear sensors in the late afternoon, we speculated that these could be caused by specular reflection on the row of PV modules behind the sensors. We included specular reflection in our modelling and compared the output with the results from another simulation where specular reflection is not used. We did not observe any contribution of the specular component of reflection on ground sensors (not shown), in good agreement with the lack of irradiance spikes. On the contrary, the simulated irradiance of part of the rear sensors represented the observation significantly better with specular reflection. This is shown in Figure 37 below.

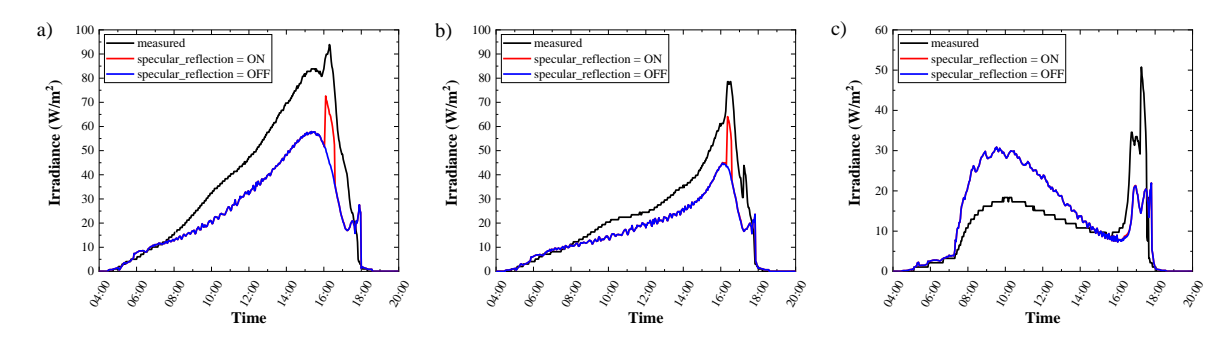


Figure 37. Effects of specular reflection for rear sensors 1 (a), 3 (b) and 8 (c). The measured data is shown with black whereas the modelled data is colour coded for specular reflection included and excluded simulations. Time scale is given as hours.

It can be seen from the figure that the spikes (with red colour) seen in the sensors in late afternoon (around 16:30) is not represented by the model that does not include specular reflection. However, when specular reflection is included, it was possible to obtain this spike, although not as strong as the measured data. This clearly indicates that specular component of reflection should be included in the model.

4.3.5 Table (simulation) size

The specular reflection, leading to irradiance spikes in the late afternoon, only occurs under very high angle of incidences on the back row of PV modules. This automatically implies that the point of reflection and the point of incidence are quite far apart in the direction of the rows. In fact, so far apart that quite soon, this point is outside of the area of the back row. With this in mind, we checked the effects of dimensions of modelled system which consists of 3 rows of tables with sensors on the



central one (see image below). We increased the size of the tables located on the east and west of the central table from 5 m to 10 m and then to 20 m. In addition, due to the finite width of the tables, light, in late summer afternoons could pass the side of the table and reach the downward looking sensors. It should be noted that increasing the table size also increased the time required for simulations significantly (to over 4.5h when 20 m long tables are used). Therefore, we did not investigate even larger table dimensions.

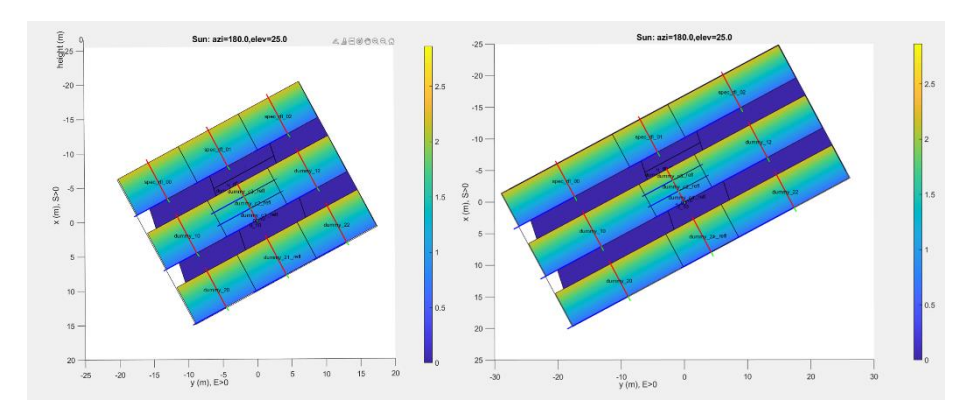


Figure 38. Image of modelled test field with 10 m (left) and 20 m (right) long tables on both sides of the central row.

With increasing simulated table sizes, we observe three major effects: (i) the cut-off at the end of the day is better represented by the model, (ii) the peak that appears in the modelled data when 5 m long tables are used, early in the morning, is not visible when the table size is increased and (iii) the peak due to specular reflection gets wider. These observations are shown in Figure 39. Clearly the larger table sizes in the simulation give a better description of the actual system on all these three effects.

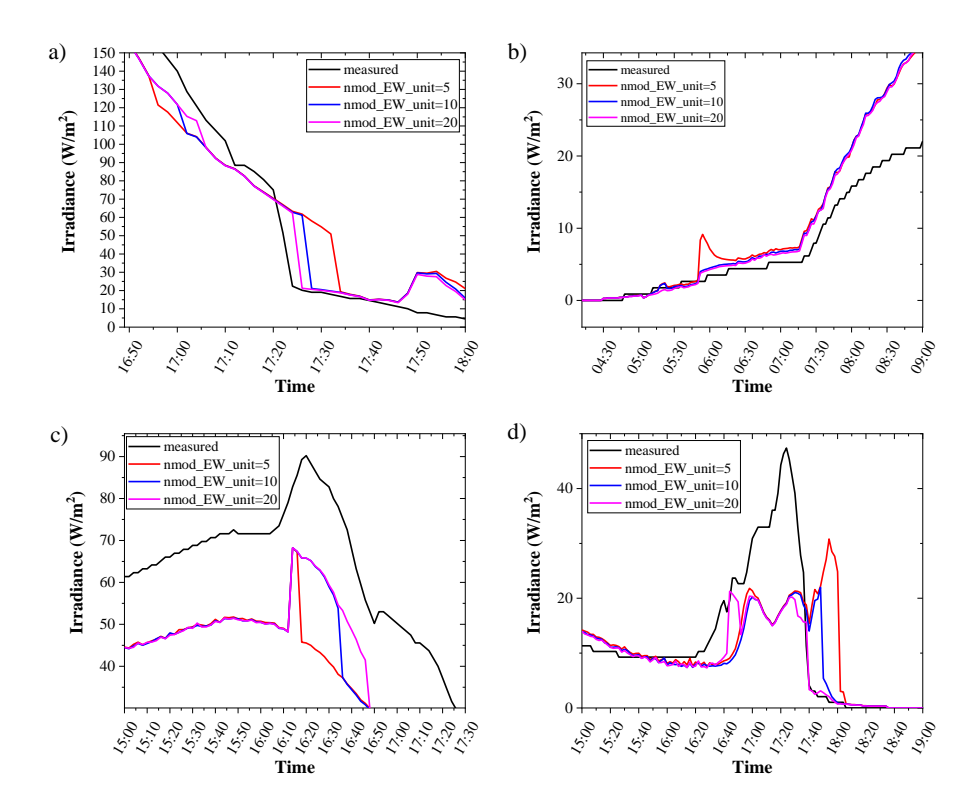


Figure 39. Irradiance vs time graphs of (a) ground sensor 2, (b) ground sensor 8, (c) rear sensor 2 and (d) rear sensor 9. (a) and (d) show better representation of end of day cut-off, (b) peak appears early in the morning disappears when wider tables are used and (c) specular reflection related reflection component becomes more effective. The width of the tables are given in the figure legends with "nmod_EW_unit". Each value corresponds to a table size in meters. Time scale is given as hours

4.3.6 Gap between modules

The solar panels are placed with 2 cm distance from each other. This means direct sun light can penetrate through the gap between the modules and hit the sensor resulting in spikes in the irradiance measurements. These spikes are observed in many of the ground sensors graphs. We have also modelled these gaps. It's important to note that BIGEYE simulates a PV panel as a plane with zero thickness. A 2 cm gap between two modules is then also a gap with zero thickness, whereas in reality the thickness of the PV laminate, about 10 mm, and, when present, the module frame, about 30-40 mm, will make the passing beam even more narrower. We have also included the gaps between the modules in the BIGEYE simulations and observe these spikes also in our modelled data as shown below. For reference, the case without gaps, and thus without spikes, is also plotted. Clearly, we do model the spikes at the right time, but overestimate the irradiance and the duration. As explained above, one reason is the two-dimensional opening in the model, compared to the three-dimensional in real life, the other reason is that in BIGEYE the sun is a point source. When it is incident on a surface, either sensor or PV, it is fully incident on that surface, whereas in real life the sun has an angular width and probably will only be partially visible through the gap.



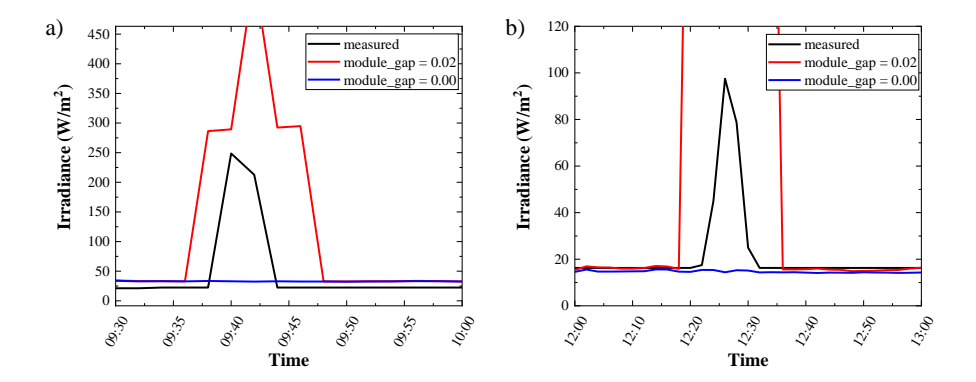


Figure 40. Effects of module gap on the modelled data for ground sensors (a) sensor 2 and (b) sensor 6. The figures illustrates that the peak observed at 09:40 is absent when no gap is used. The measured data is shown with black whereas the modelled data is colour coded for each module gap value. Time scale is given as hours.

4.3.7 Sources of rear and ground irradiance

Although ultimately all light originates from the sun, it does not always reach the PV tables and irradiance sensors directly. BIGEYE uses a view-factor method to determine if the sun or a part of the sky contributes to the irradiance on front or rear side of objects. The same holds for reflected light, both from the ground, albedo, as from (specular)reflecting objects like other PV panels or mounting structure. We have separated the total irradiance on two sets of sensors. Figure 41 shows the resulting stacked irradiance for rear side sensors, numbers 1, 6 and 10. Note that the indirect irradiance, denoted "dome_fr", is present but more or less uniform over the day. The more or less uniform daily total "dome_fr" irradiance is about 70% of the daily total, "beamCS_fr" irradiance, which is concentrated in two peaks.

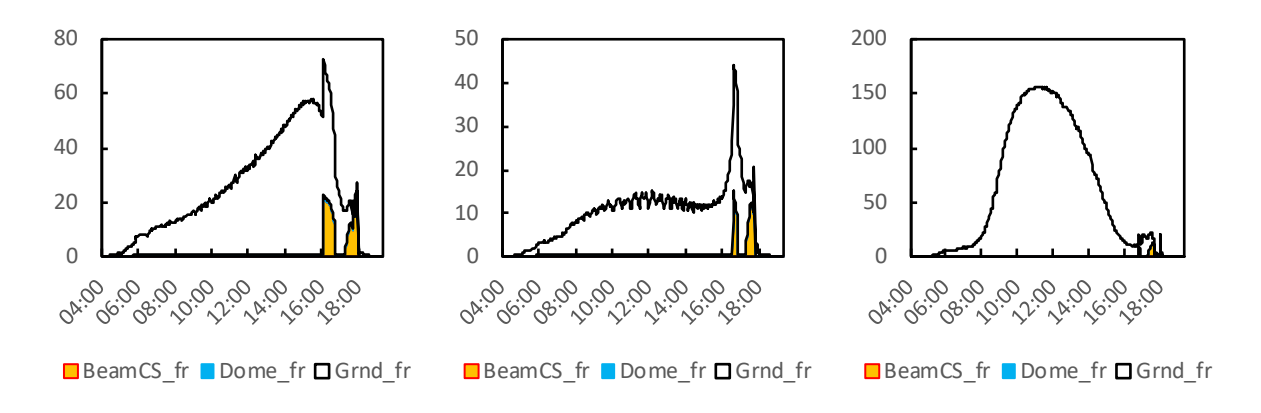


Figure 41. Irradiance on the rear side of the PV panels, separated in direct, indirect and ground-reflected as origin. The first direct light peak is specularly reflected on the front glass of the back row of PV panels, the second peak is direct irradiance on the back of the PV panels.

A similar analysis is made for the sensors on the ground. Figure 42 shows the resulting stacked irradiance for the sensors, 1, 6 and 10 on the ground. Sensor 10 is located in front of the lower edge of the PV table and thus observes direct irradiance for most of the day. The horizon brightening (or darkening) is a minor contribution, but most pronounced in the ground sensors in the centre of the PV table. The reflected light becomes more prominent when the direct (and indirect) irradiance is smaller and the distance between the PV table and the ground is shorter. For sensor 6 back sheet reflected light is the largest contributor to its total irradiance, although the sharp peak, around 12:00, of the beam passing in between two solar panels looks dominant.



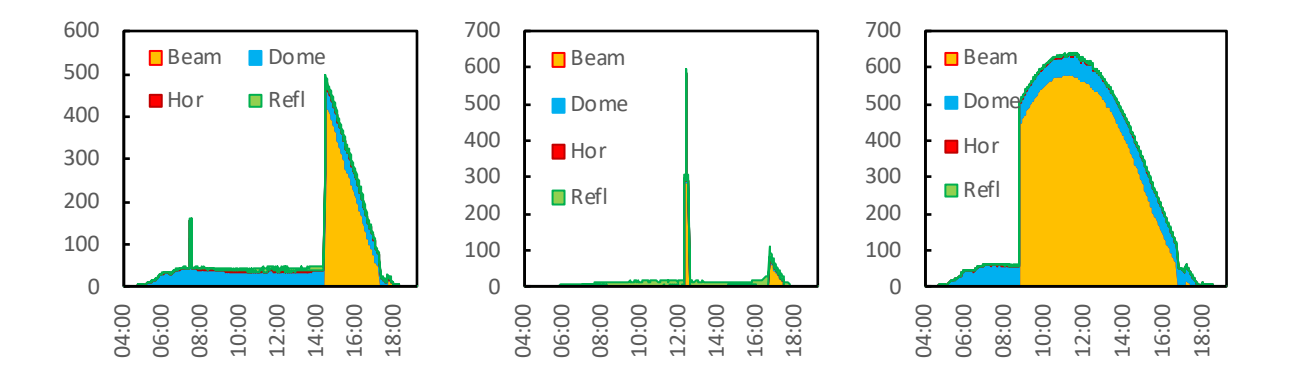


Figure 42. Irradiance on the ground below the PV panels, separated in direct, indirect, horizon and reflected as origin. Reflected light refers to the scattering of light on the white back sheet side of the PV table.

4.4 Conclusions

In this Project, we extended TNO's solar farm software package BIGEYE with two optical improvements. We can now simulate specular reflection at solar panels. We have also found a method to include the (diffuse) reflection of light on the rear of back sheet modules. We also experimented with a variable albedo on the ground. This is a useful addition for running and future projects that involve nature inclusive solar parks and agrivoltaic solar farms. There we expect a different ground coverage, e.g. strips with herbs directly under the solar panels and cropland, that varies from bare soil to fully covered green or yellow crops.

With these additions, we have shown how well we understand the optics, around and below solar panels in a commercial solar farm. We have applied this knowledge to calculate more accurately the effects of module properties and system design on the energy generation and the ground irradiance. The consideration how densely a solar farm can be packed to maximise financial gain and maximise renewable energy generation or how open such a system should be not to damage the soil is a combination of policy and considering the numbers. We can now supply these numbers, but we cannot determine whether the coverage should be 75%.

What we can recommend is that both the energy yield calculations and the ground irradiance simulations show the best performance for the semi-transparent bifacial module. This means that for a given minimum irradiance or minimum kWh per unit area demand, with a bifacial module you can achieve the soil quality with a higher coverage of solar panels. Alternatively, you can achieve the energy performance demand with fewer modules per area due to the bifacial gain and have a higher soil irradiance.



5 Business modelling

5.1 Land based solar

When bifacial modules are used, light reaching the rear side of modules can have a significant contribution to annual yield. As we have learnt from the previous chapter, the choice for different back sheets has an influence on the illumination under the modules. Bifacial modules usually have transparent back sheets, which has a direct influence on the light reaching the soi. Furthermore, the ground coverage of the system influences the light reaching the rear side of the modules. Using the model improvements developed in this project, we calculated the energy yield and the ground irradiance under the module using different back sheets and different ground coverage ratios.

5.1.1 Assumptions

Specular reflection contributes about 1.1% irradiance to the rear irradiance and 0.2% to the ground irradiance. In this case, the rear irradiance adds 10% to the annual irradiance on the PV without specular reflection, adding the specular reflection increases this addition to 10.1% of the front irradiance. This will have no significant effect on the business case for bifacial, semi-transparent solar parks. Therefore, for this section specular reflection will not be used.

5.1.2 Results

With the improved knowledge and software parametrisation, we can now calculate the annual energy yield for a solar park and at the same time calculate the effect on the ground irradiance as measure for the risks or benefits to the soil quality. To make this more insightful, we varied the ground coverage ratio, as well as the module type. Three types are considered: 1) regular white back sheet modules, 2) black back sheet modules and 3) semi-transparent bifacial modules. The ground irradiance, labelled soil, is expressed in percentage of the open field annual irradiance, about 1000 kWh/m² in the Netherlands.

Yield	80%	67%	50%
WBS	10581	11377	11715
BBS	10580	11362	11715
TBS	10772	11643	12065

soil	80%	67%	50%
WBS	20%	32%	49%
BBS	18%	30%	47%
TBS	24%	36%	52%

WBS: white back sheet; BBS: black back sheet; TBS: transparent back sheet.

The data above are for the same system size in nominal capacity. Clearly, with more spacing between the modules, that is lower coverage ratio, the energy yield per kWp increases. Also the average irradiance on the ground increases. In first order, the average ground irradiance is 100% minus the coverage ratio, but we see that the module type has also an effect. Clearly, the semi-transparency increases the ground irradiance by about 6% absolute compared to the black back sheet case, where no light passes through the PV modules. Compared to the black back sheet, the white back sheet has the additional contribution of reflecting part of the albedo light back to the ground. This effect is about a third of the transparency effect.

yield per area	80%	67%	50%
WBS	8464	7623	5858
BBS	8464	7613	5858
TBS	8617	7801	6032

But of course, the energy generation per unit area decreases strongly with decreasing coverage. The coverage is the leading aspect here, with the increased yield per panel much weaker. Finally, we note that there is little to no difference between the two monofacial module types, but the bifacial, semi-

41



transparent one clearly has a higher energy output, which increases with lower coverage as the ground irradiance increases at the same time.

5.2 Floating solar

Using the insights gained in this project and the developed thermal model for floating PV module temperatures, we simulated the energy output difference of land based and floating solar energy systems.

5.2.1 Assumptions

From our study we see that the correlation between PV module temperature and the ambient temperature on one hand, and the PV module temperature and the water temperature are not independent. Therefore we choose not to use a yield model that takes both the ambient temperature (c_1) and the water temperature (c_7) into account, but a model that only uses the ambient temperature (c_3) and the wind speed (c_7) . From our detailed discussion we find that the c_1 values for land and water are virtually the same, whereas we find a small increase in c_3 , with a (mean) value of 4.2 Ws/m³K for land, and 6.9 Ws/m³K for water.

5.2.2 Results

The specific yield in kWh/kWp of a land based and floating East-West PV system has been modelled. As an input measured irradiance and meteorologic conditions for the year 2021 were used. In Figure 43 the monthly specific yield of both of these systems together with the difference (Floating - Land based system) can be found. In Table 9 the annual yield can be found of these systems together with the modelled annual yield with an undersized inverter (50% rating compared to installed DC power). The relative difference in yield between FPV and land based systems decrease with an under sizing of the inverter.

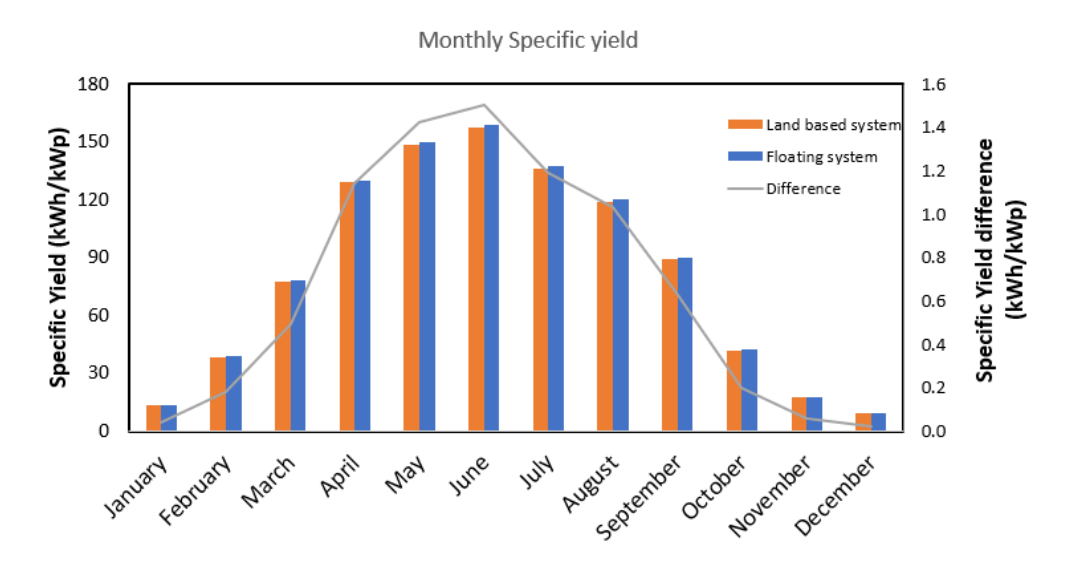


Figure 43. Modelled monthly specific yield of an East-West land based and floating system (AC to DC inverter capacity is 100%)



AC to DC inverter	Specific Annual Yield	Specific Annual Yield	Difference in yield
capacity	Land based system	Floating system	FPV vs Land based
	(kWh/kWp)	(kWh/kWp)	(%)
100%	979	987	0.8
50%	868	871	0.3

Table 9: Annual modelled specific yield of land based and FPV system based on the heat loss coefficient as determined within this work.

We find an energy output difference of 0.8% when the AC to DC conversion capacity is 100% of the rated power of the modules. In the current practice the AC to DC conversion capacity is chosen to be lower, leading to clipping during high-irradiance conditions. When we choose an inverter capacity of 50% of the rated power of the modules, the increase in output due to better cooling of floating PV systems decreases to 0.3%.



6 Appendix A – Availability all individual sensors Weperpolder

